HHS Public Access

Author manuscript

Nat Biomed Eng. Author manuscript; available in PMC 2021 April 13.

Published in final edited form as:

Nat Biomed Eng. 2020 April ; 4(4): 446–462. doi:10.1038/s41551-020-0539-4.

Human cardiac organoids for the modelling of myocardial infarction and drug cardiotoxicity

Dylan J. Richards[1,10], **Yang Li**[1], **Charles M. Kerr**[2], **Jenny Yao**[1,11], **Gyda C. Beeson**[3], **Robert C. Coyle**[1], **Xun Chen**[1], **Jia Jia**[1], **Brooke Damon**[1], **Robert Wilson**[4], **E. Starr Hazard**[5], **Gary Hardiman**[5,6,12], **Donald Menick**[7,8], **Craig C. Beeson**[3], **Hai Yao**[1], **Tong Ye**[1,*], **Ying Mei**[1,9,*]

[1]Bioengineering Department, Clemson University, Clemson, SC 29634, USA

[2]Molecular Cell Biology and Pathology Program, Medical University of South Carolina, Charleston, SC 29425, USA

[3]Department of Drug Discovery and Biomedical Sciences, Medical University of South Carolina, Charleston, SC 29425, USA

[4]Department of Pathology and Laboratory Medicine, Medical University of South Carolina, Charleston, SC 29425, USA

[5]MUSC Bioinformatics, Center for Genomics Medicine, Medical University of South Carolina, Charleston, SC 29425, USA

[6]Departments of Medicine and Public Health Sciences, Medical University of South Carolina, Charleston, SC 29425, USA

[7]Division of Cardiology, Department of Medicine, Gazes Cardiac Research Institute, Medical University of South Carolina, Charleston, SC 29425, USA

[8]Ralph H. Johnson Veterans Affairs Medical Center, Medical University of South Carolina, Charleston, SC 29425, USA

[9]Department of Regenerative Medicine and Cell Biology, Medical University of South Carolina, Charleston, SC 29425, USA

[10]Current address: Janssen Pharmaceuticals Inc., Johnson & Johnson, Spring House, Pennsylvania, 19477

[*]Corresponding authors, ye7@clemson.edu; mei@clemson.edu.

Author contributions

D.J.R., T.Y. and Y.M. conceived the study with assistance from D.M.; D.J.R., Y.L., C.M.K., B.D., and J.Y. designed the experiments with C.C.B., H.Y., T.Y and Y.M.; D.J.R. supervised all experiments, led the data analyses and manuscript preparation with Y.M. Diffusion modeling was performed by R.C.C. and J.Y.; D.J.R. performed all immunofluorescent staining, confocal imaging, and image analysis with assistance from J.J. and C.M.K.; D.J.R. performed all RNAseq/microarray analysis of organoid and public data sets, including meta-analysis, PCA, and GSEA. R.W., E.H., and G.H. performed RNA sequencing, quality control of RNAseq output, and managed Advaita Bio input. C.M.K., G.C.B. and C.C.B. performed Seahorse metabolic experiments and analysis. H.Y., B.D., and J.Y. designed micropipette aspiration apparatus. D.J.R., J.Y. and C.M.K. performed mechanical testing and analysis. Y.L., X.C., H.Y. and T.Y. developed customized two-photon scanned light-sheet microscope. D.J.R. and Y.L. performed all multi-photon and customized two-photon scanned light-sheet microscope imaging and analysis. G.H., D.M., C.C.B., H.Y., T.Y. and Y.M. supervised the efforts, including the manuscript preparation.

Competing interests

The authors declare no competing interests.

[11]Current address: Department of Physics, Harvard University, Cambridge, MA 02138, USA

[12]Current address: School of Biological Sciences, Institute for Global Food Security, Queen's University Belfast, Belfast BT9 5AG, UK

Abstract

Environmental factors are the largest contributors to cardiovascular disease. Here, we show that cardiac organoids incorporating an oxygen-diffusion gradient and stimulated via the neurotransmitter norepinephrine can structurally model the human heart after myocardial infarction (mimicking the gradient of infarct, border, and remote zones), and recapitulate hallmarks of myocardial infarction (such as pathological metabolic shifts, fibrosis and calcium handling) at the transcriptomic, structural and functional levels. We also demonstrate that the organoids can model hypoxia-enhanced doxorubicin cardiotoxicity. Human organoids that model diseases with non-genetic pathological factors could aid drug screening and development.

Human induced pluripotent stem cells (iPSC) and adult stem cells (aSC) provide an ideal cell source to study human development, disease modeling and drug testing.[1–3] To this end, significant efforts have been devoted to human organoid systems, as they provide a biomimetic microenvironment (e.g., 3D spatial organization, multiple cell types, organ-specific function/structures) to recapitulate cell-cell and cell-matrix interactions of a variety of tissues.[3–5] These human organotypic 3D microtissues have synergized with recent advances in genetic engineering to greatly accelerate our understanding of the contributions of genetic factors in major diseases, including cancer, neurological, liver, and intestinal disorders.[3,4,6–11]

Cardiovascular disease (CVD) is the leading cause of death worldwide, yet to date, there has been limited progress in the development of human cardiac organoids for CVD modeling.[12] Meanwhile, significant progress has been made in the use of stem cell-derived cardiomyocyte-based cardiac microtissues/organoids for studying maturation, improving cell therapy, and drug/toxicity studies.[13–17] In addition, major efforts have advanced the understanding of congenital cardiomyopathies and genetic pre-dispositions to cardiotoxicity using iPSC-derived cardiomyocyte (hiPSC-CM) systems.[18–23] However, the largest attributable factors of CVD are non-genetic, such as lifestyle and environment.[12] This highlights the translational opportunities of human cardiac organoids to study CVD with non-genetic causes, like myocardial infarction (MI) (i.e., heart attack). Heart attacks make up ~8.5% of CVD and are a common cause of heart failure with a 40% five-year mortality after the first MI.[12] While the re-establishment of blood flow and targeting of neurohormonal pathways has significantly improved post-MI survival[24], there has been limited success in heart failure clinical trials during the past decades, which has been partially attributed to the disconnect between basic research findings using animal models of heart failure and human patients.[25–27] Despite advancements in understanding the injured heart after MI in animals, research surrounding the human myocardium after MI has been limited to chronic end-stage ischemic cardiomyopathy (given the availability of donor tissue) and in vitro human models of related cellular mechanisms (e.g., adrenergic stimulation, cell death from reperfusion).[13,16,28–30] Although engineered constructs have

been used to evaluate immediate (i.e., minutes, hours) effects of low oxygen environments[16,31], there is a lack of human models that recapitulate the organotypic features (e.g., tissue remodeling) of the short-term (i.e., days) post-MI injured state of cardiac injury. This stage is critical in understanding the acute post-infarct heart tissue caused by either ischemia or ischemia/reperfusion (I/R) and is difficult to obtain and study in humans.[13,32] In addition, cardiotoxicity is a major concern for pre- and post-approval in the development for all systemically-delivered drugs.[33] Specifically, the ability to detect drug-induced exacerbation of cardiotoxicity is an unmet need for all drug development to address safety concerns for patients with pre-existing cardiovascular conditions, as CVD is a common comorbidity of major diseases.[33–36]

Here, we combined major non-genetic causal factors of MI with our previously established human cardiac organoids to create an in vitro 3D model of the post-MI myocardial tissue.[31,36–40] Whereas previous cardiac 2D/3D systems have contributed to the understanding of effects of individual MI-related factors (e.g., hypoxia, adrenergic stimulation, substrate mechanics) in homogenous (i.e., no gradient) environments[13,31,36–40], we leveraged nutrient transport principles (namely, oxygen diffusion) in 3D microtissues along with chronic adrenergic stimulation to create a gradient of “apoptotic center-dysfunctional interior-functional edge” in human cardiac organoids, which recapitulated the “infarct-border-remote zones” of infarct hearts.[41–43] This allowed us to mimic organotypic myocardial response to infarction in cardiac organoids, where the behaviors of multiple cell types with varied structures/functions across 3D space are critical to model disease hallmarks of acute post-MI hearts (i.e., fibrosis and pathological calcium-handling). Meta-analysis of the transcriptomic changes in the human cardiac infarct organoids showed high similarities with transcriptomes of acute post-infarct tissue from animal models of MI and human ischemic cardiomyopathy, supporting the overall relevance of this model. Major post-MI hallmarks identified at the transcriptomic level were then validated through structural and functional analysis, including in-situ imaging of calcium dynamics inside 3D cardiac microtissues with a custom two-photon scanned light sheet microscope. Moreover, the translational strength of this model was demonstrated by tissue-level heart failure drug testing and drug-induced exacerbation of cardiotoxicity studies.

Results

Development of human cardiac infarct organoids.

During a heart attack, a blocked artery limits the delivery of oxygenated blood to downstream myocardium causing massive cell death, leading to reduced ability to pump blood to the body that triggers compensatory efforts by the nervous system to restore cardiac output (i.e., adrenergic stimulation via norepinephrine).[44] Given the inability of the damaged heart to fully compensate or regenerate, this positive feedback causes heart dysfunction and ultimately heart failure.[44] With the understanding of major upstream causal factors in MI-associated injury, we leveraged inherent oxygen diffusion gradients in 3D microtissues and chronic adrenergic stimulation to model the organotypic response of myocardium after infarction with human cardiac organoids (Fig. 1a).[41,42] To gain insight into oxygen distribution in cardiac organoids and provide a guiding design principle for an “organoid

infarction" protocol, a mathematical diffusion model was constructed using a 150 μm radius cardiac microtissue.[45] In contrast to normoxia (20% oxygen), the microtissue in hypoxia (10% oxygen) experiences a gradient of viable to non-viable oxygen levels from edge to center (Fig. 1b, 1c), mimicking the gradual change in nutrient availability (in this case, oxygen) in infarcted hearts.[46] Applying this model as a guiding design principle of reduced oxygen environment toward the organoid center, cardiac organoids with a radius of ~150 μm cultured at 10% O_2 with 1 μM norepinephrine (NE) (i.e., infarct organoids) for 10 days showed a higher intensity of hypoxia staining at the interior of live-imaged organoids compared to organoids cultured in control conditions (Fig. 1d–1f). In addition, infarct organoids showed apoptotic TUNEL+ staining in the center of organoid sections, attributed mainly to the non-viable oxygen levels at the center of the organoids (Fig. 1g). This was also supported by a further decrease in TUNEL index at the interior of organoids after 10 days of 10% O_2 only compared to 10 days of 1 μM NE only (Fig. S1a, S1b). Two-photon imaging of live organoids also showed decreased NADH autofluorescence at the interior of the control organoids and across infarct organoids, supporting the reduced oxygen environment in the center of organoids and in infarct organoids (Fig. 1h).[47] The infarct organoids also showed a NE-induced increase in beat rate, which was reversed when cultured with 10 μM metoprolol beta-adrenergic blocker (Fig. S1c).

It is worth noting that our approach seeks to leverage a gradient of oxygen to create a functional gradient across organoids (i.e., apoptotic center-dysfunctional interior-functional edge) to mimic the "infarct-border-remote zones" of post-MI hearts. This is in great contrast to previous research that use anoxia/hypoxia (e.g., 0% or 1% O_2) as a homogenous (i.e., no gradient) stimulus to evaluate its effect on cell function. For example, 10 days of 0.1% O_2 (with 1 μM NE) culture of cardiac organoids resulted in microtissues with a fibrotic shell (vimentin+) and apoptotic core (TUNEL+), as well as the complete loss of hiPSC-CMs (lack of αSA+ sarcomeric banding and no contractile function) (Fig. S1d). This demonstrates the advantage of using a gradient-generating level of oxygen (i.e., 10%) instead of using a homogeneous hypoxia treatment (e.g., 0.1% O_2 in this study) to create a functional tissue-level model of the post-infarct state.

Transcriptomic meta-analysis of cardiac infarct organoids.

To examine the global downstream effects of the cardiac organoid infarction protocol (i.e., 10% O_2 and 1 μM NE treatment) on gene expression, the transcriptomes from the control and infarct organoids were analyzed using RNA sequencing (RNA-seq) and resulting data was submitted to the NCBI Gene Expression Omnibus under accession number designation GSE113871. The cardiac organoid infarction protocol resulted in 5,675 differentially expressed (DE) genes ($p < 0.05$) compared to control organoids (Fig. 2a). The translational potential of the cardiac organoid infarction method for modeling human post-infarct cardiac tissue is dependent on its similarity to adult ventricular tissue after ischemic cardiac injury from clinical and preclinical studies. When compared to ischemic cardiac injury transcriptomic data from public human (i.e., human ischemic cardiomyopathy, ICM) and animal (i.e., 1 wk post-MI) studies, infarct organoid DE genes overlapped with >1,000 genes of human, mouse, and porcine DE genes, similar to the overlap between animal MI models and human ICM samples (Fig. 2b, S2a). The gene ontology of the overlapping regions was

indicative of ischemic cardiac injury, including terms such as “response to oxidative stress”, “heart contraction”, and “fibroblast proliferation” (Table S1).

Whole transcriptome comparison between the organoid, human, and mouse data was performed using principal component analysis (PCA). After PCA of the 4,765 shared genes from the organoid data and two public RNA-seq datasets of human ICM and mouse MI (2 wks), the top PCs showed visible separations between samples (Fig. 2c, S2b, S2c). In efforts to gain a functionally meaningful interpretation of these visual patterns, gene set enrichment analysis (GSEA) was used with the gene list and PC gene loadings as ranks (Table S2). PC1 visualized the global transcriptomic variation between species, where organoid samples grouped with human samples separate from mouse (Fig. 2c), which was supported by secondary analysis using control mouse heart RNA-seq data from a different sequencing platform (Fig. S2d). This separation of species and high proportion of variance (50.6%) of PC1 highlighted the potential translational insight of using a human in vitro organoid system to model aspects of human cardiac injury. PC2 separated heart tissue samples (positive) from cardiac organoid samples (negative), attributed to differences in tissue complexity, where immune system and developmental process terms were enriched in positive and negative PC2 gene loadings, respectively (Fig 2c, Table S2). Plotting PC3 versus PC4 visualized a clear grouping of injury samples relative to controls across the x-axis (PC3), while PC4 showed separate grouping patterns of mouse and organoid control/injury samples in contrast to a lack of separation of human control and ICM samples across the y-axis (PC4) (Fig. 2d). Gene ontology analysis of loadings-ranked PC3 genes supported the ischemic cardiac injury-like phenotype (e.g., extracellular matrix, leukocyte migration, TGF-beta receptor binding) of injury samples (negative) and physiological phenotype (e.g., cellular respiration, regulation of conduction) of control samples (positive) (Table 1, Table S2). PC4 characterization revealed that mouse and organoid injury samples shared positive PC4 coordinate locations with associated functional terms indicative of acute post-infarct injury (e.g., regulation of inflammatory response, cell chemotaxis), while the human injury samples had dispersed coordinates along PC4 (Table 1, Table S2), attributed to their large biological variation (e.g., time after injury, disease severity, tissue isolation method, age). By incorporating human and mouse heart failure data, PCA delineated the dimensions where relevant pathological similarities exist (PC3, PC4), yet acknowledged inherent differences between species and tissue complexity (PC1, PC2). The transcriptomic meta-analysis of human control and infarct organoids as well as ischemic heart failure data from multiple species established a systems-level relevance of the cardiac infarct organoids in modeling injured myocardium, and more specifically acute post-infarct ventricular tissue that can be subsequently tested for functional validation.

Pathological metabolic shifts in cardiac infarct organoids.

Given the translational relevance of this work, we next investigated specific post-MI characteristics observed in the organoid infarction model. Pathway analysis of DE genes in infarct organoids showed top hits that included “carbon metabolism” ($p = 5.24 \times 10^{-6}$), “citrate cycle (TCA)” ($p = 9.25 \times 10^{-6}$), and “glycolysis/gluconeogenesis” ($p = 1.67 \times 10^{-3}$) (Fig. 3a, S3a). Notably, transcriptomic shifts of DE genes in “metabolic pathways” (KEGG pathway map01100), a large pathway term including several metabolic modules, in infarct

organoids were consistent with data from mouse 1 wk post-MI samples (Fig. 3b, Table S3). These changes supported a biomimetic shift towards anaerobic metabolism due to the organoid infarction protocol. Seahorse mitochondrial stress tests on individual organoids revealed a ~2-fold increase in the oxygen consumption rate (OCR) of control organoids after FCCP treatment (Fig. 3c), indicating their physiologically relevant metabolism.[48] The infarct organoids showed a significantly reduced OCR response to FCCP treatment compared to control organoids (Fig. 3c, 3d), suggesting impaired mitochondrial function and oxidative phosphorylation. Oligomycin treatment led to a ~30% increase in the extracellular acidification rate (ECAR) of infarct organoids compared to control organoids (Fig. 3e, 3f). This was accompanied by a biomimetic accumulation of L-lactate in infarct organoid media (Fig. 3g), which was attributed to the enhanced lactic acid production, supported by the increased ratio of LDHA:LDHB and decreased ratio of SLC16A1:SLC16A3 in infarct organoids (Fig. 3h).[46,49–53] This evidence strongly supports a shift towards glycolytic metabolism in infarct organoids. The transcriptomic data combined with functional analyses showed that infarcted organoids recapitulate key aspects of metabolism in human infarcted myocardium.

Cardiac infarct organoids display pathological fibrosis.

Fibrosis is one of the central hallmarks of injured cardiac tissue in human MI and animal MI models.[54] Fibrotic gene and cellular phenotypic (myofibroblast-like) shifts have been observed in the acute temporal range after MI in a number of animal models.[28,29,55] While evidence of acute fibrosis in primates (nonhuman and human) is often from hypertrophy models and clinical indicators of fibrotic activity (e.g., delayed-enhancement imaging), these temporal and pathological differences between species further supports the use of cardiac infarct organoids to explore human cardiac fibrosis in the context of infarction injury.[56–59] Comparing infarct to control organoids, gene ontology analysis of DE genes indicated top significant biological processes related to multicellular interactions and extracellular matrix (ECM) and top pathway hits of “ECM-receptor interaction” ($p = 5.32 \times 10^{-7}$) and “dilated cardiomyopathy” ($p = 9.81 \times 10^{-6}$) (Fig. 4a, S3a, S3b). An assembled fibrosis-related gene set, containing genes related to cell adhesion/migration (e.g., ITGB3), ECM (e.g., COL1A1), growth factors (e.g., TGFB1), and protease/inhibitor (e.g., MMP2) (Table S4), showed an overall increase in fibrosis-related gene expression in infarct organoid samples, consistent with data from mouse 1 wk post-MI samples (Fig. 4b–4d, Table S4). While fibrotic gene shifts may have partially resulted from the increased fibroblast to cardiomyocyte ratio due to death of cardiomyocytes, these changes are typical for the damaged regions of the heart in vivo as well and thus support tissue-level transcriptomic comparisons (i.e., organoids and mouse heart tissue).

The transcriptomic changes indicated a biomimetic fibrosis-like downstream response within infarct organoids. This data was further characterized by structural analysis of fibroblast cellular organization. Vimentin staining was used for general labeling of mesenchymal cell types (e.g., fibroblasts) and to characterize the fibroblast behavior in the organoids. Infarct organoids showed a significant shift in vimentin+ organization (i.e., fibroblasts) toward the edge of the organoid compared to control organoids, seen by confocal imaging and radial density profile plots of vimentin+ area in organoid frozen sections (Fig. 4e, 4f, Table S5).

The presence of myofibroblasts is commonly used to histologically identify fibrotic tissue in the infarcted heart.[54] Alpha smooth muscle actin (αSMA) in combination with phalloidin staining of F-actin was used as a standard method to identify the presence of myofibroblast-like cells, specifically marked by αSMA+/F-actin+ co-staining in a distinct fibrillar structure that is not seen in nonfailing/control tissue samples. Infarct organoids showed numerous myofibroblast-like structures, marked by elongated, αSMA+/F-actin+ phenotype in contrast to control organoids (Fig. 4g, S4). The presence of myofibroblast-like cells and associated fibrotic gene profile suggested a change in the organoid mechanical environment.[60] A micropipette aspiration method was adapted for microtissues to measure the elastic modulus (i.e., stiffness) of the outer viable regions of the cardiac organoids.[61] The stiffness was significantly increased in infarct organoids over control organoids (Fig. 4h, 4i). The observed stiffness changes are similar to mechanical changes seen in infarcted and fibrotic myocardial tissue.[62] Notably, the changes in stiffness after formation of a mature scar can be much higher than the ones we observed here. In vivo studies have shown that mechanical changes in injured fibrotic hearts in acute MI reflect the total effect of fibroblast-associated changes (e.g., cell density, total ECM deposition/remodeling).[39,62] Supporting this, mechanical testing of newly formed microtissue variants showed that fibroblast (FB) spheroids had higher stiffness than cardiomyocyte (CM) spheroids, and cardiac organoids with 10% more FBs (organoid+FB) were stiffer than cardiac organoids (Fig. S5).

With the timeline of our model (i.e., 10 days), the change in the tissue-level mechanical properties, fibrotic transcriptomic shifts parallel to mouse 1 week post-MI myocardium, and presence of αSMA+ myofibroblast-like cells corroborate an endogenous fibrosis response in infarct organoids that mimics characteristics seen in vivo. While previous studies have required fibroblast monoculture, the addition of TGF-β1, and/or direct changes to culture material properties (e.g., substrate stiffness) to investigate fibrotic/myofibroblast behavior[31,37,38,63], of the cardiac organoid infarction method led to endogenous increases in myofibroblast-like cells and corresponding increase in tissue stiffness in cardiac organoids as a result of biomimetic upstream pathological stimuli (i.e., hypoxia gradient and norepinephrine), supporting the relevance of the organoid model for cardiac infarction.

Pathological calcium-handling in cardiac infarct organoids.

In addition to fibrosis, calcium handling changes associated with MI serve as a functional hallmark of post-infarct cardiac injury.[64] Pathological calcium handling is linked to contractile dysfunction and contributes to the occurrence of arrhythmias after MI.[65] At the transcriptomic level, “ion transport” ($p = 2.10 \times 10^{-7}$) was a top ten gene ontology term between control and infarct organoids, and top pathway hits included “calcium signaling pathway” ($p = 8.85 \times 10^{-7}$) and “arrhythmogenic right ventricular cardiomyopathy” ($p = 4.18 \times 10^{-5}$), indicative of changes in calcium handling (Fig. 5a, S3a, S3b). The “calcium signaling pathway” KEGG term 4020 was used to assemble a calcium handling-related gene set (Table S6). After filtering for the calcium handling-related gene set, infarct organoids showed an overall consistency with calcium handling gene expression of 1 wk post-MI mouse heart samples, including significant decreases in well-studied calcium-handling components ATP2A2 (sarco-endoplasmic reticulum Ca^{2+}-ATPase), RYR2 (ryanodine receptor), CACNA1C (L-type calcium channel), SLC8A1 (sodium-calcium exchanger), and

increase in ITPR3 (inositol 1,4,5-trisphosphate Receptor Type 3) (Fig. 5a–5c, Table S6). Although these changes cannot be solely attributed to cellular gene expression given decreases in other cardiac specific genes (Fig. S6), the similarity to post-MI mouse hearts (Table S6) suggested biomimetic pathological calcium handling within infarct organoids.

To functionally interpret the transcriptomic shifts in calcium handling, we developed a customized Two-Photon scanned Light-Sheet Microscope (2PLSM) that created a thin sheet of illumination by scanning a laser beam laterally and imaged the illuminated area with a high-speed camera.[66] The deep penetration of two-photon excitation allowed the imaging plane to be positioned across the interior region of the organoid[67], and the high-speed camera recorded calcium events in the illumination plane (~4 μm thickness section) with high temporal resolution (20 ms) (Fig. 5d, S7a, S7b). The 2PLSM allowed for the visualization of calcium handling in the interior regions of 3D cardiac microtissues to study calcium handling and arrhythmogenicity across the organoids. Calcium transient amplitudes ($\Delta F/F_0$) of the organoids fabricated with GCaMP6-labeled hiPSC-CMs were measured from "cell-sized" regions of interest (ROIs) (representing individual cardiomyocytes). 2PLSM imaging of control organoids displayed synchronized beating with an interconnected cardiomyocyte network (Fig. 5e - *top*, Video S1). In contrast, 2PLSM imaging of infarct organoids revealed notable unsynchronized beating profiles (i.e., arrhythmias) between separated cardiomyocyte populations at the interior and the edge of infarct organoids (Fig. 5e - *bottom*, Video S2). These observations were also seen in bright-field videos (Video S3, Video S4). Interior cardiomyocytes in the infarct organoids showed significantly lower max calcium transient amplitude in contrast to the infarct and control edge cardiomyocytes (Fig. 5f). The reduction in calcium transient amplitude is consistent with the significant changes in gene expression of calcium-handling related genes in infarct organoids that decreased in the same manner as mouse MI samples and supports cellular level pathological calcium-handling. Contraction amplitude was also significantly reduced in infarct organoids compared to control organoids, further supporting the effect of reduced biomimetic calcium handling changes on contractile function (Fig. 5g). The difference in calcium synchronization between control and infarct organoids was supported by segregated αSA+ cardiomyocyte populations in infarct organoids in contrast to interconnected αSA+ cardiomyocytes in control organoids (Fig. 5h). We reasoned that fibrosis (i.e., vimentin+ cell-associated changes) separated interior cardiomyocytes in infarct organoids into an unsynchronized, smaller beating population that experiences hypoxia-induced aberrations in calcium handling, consistent with the in vivo fibrosis-related contributions to ventricular arrhythmia post-MI.[65,68] This was supported by hiPSC-CM-only spheroids (i.e., without fibroblasts) cultured in the organoid infarction protocol that showed no indication of unsynchronized beating nor differences in edge-interior calcium transient amplitudes (Fig. 5i, S8, Video S5).

Non-genetic basis of cardiac infarction injury.

Considering the large contribution of non-genetic factors to the downstream effects post-MI, we hypothesized that changing the genetic background of cardiac organoids would not significantly alter the major hallmarks we observed in cardiac infarct organoids. Analysis of cardiac organoids using hiPSC-CMs from a different donor (i.e., Donor B, GSE115031)

revealed significant genetic background differences between Donor A and B organoids in PC1 (Fig. S9), while showing similar transcriptomic shift due to the cardiac organoid infarction protocol in PC2 (Fig. S9, S10). Structural and functional analysis confirmed the hallmark post-MI downstream effects, including fibrosis-like tissue phenotypes and the presence of unsynchronized calcium transients in infarct organoids in contrast to control organoids, supporting the non-genetic basis of the organoid infarction injury (Fig. S11, S12, Video S6–S9).

Tissue-level heart failure drug testing.

For translational applications, the cardiac infarct organoids established here provides a tissue-level human MI model for drug screening. Application of an epigenetic heart failure drug candidate with recent anti-fibrotic indications, JQ1 bromodomain inhibitor[69], to infarct organoid culture significantly reduced the vimentin+ density at the infarct organoid edge and resulted in a decrease in stiffness compared to infarct organoids (Fig. 6a–6c, Table S5), consistent with reduced fibrosis observed in a mouse model of MI.[69] Given the change in vimentin staining toward the organoid edge, we hypothesized this would reduce the fibrosis-induced separation of cardiomyocytes and increase synchronized beating in infarct organoids. This was evidenced by a reduction in the occurrence of unsynchronized beating in infarct organoids treated with JQ1 where synchronized infarct organoids treated with JQ1 showed a lack of unsynchronized interior population of cardiomyocytes (Fig. 6d, 6e, Video S10). The effect of JQ1 on both the fibrotic response and cardiomyocyte beating behavior supports the translational strength of a 3D cardiac infarct organoid model beyond 2D cell systems for tissue-level insight into heart failure drug candidate testing that can be observed at structural, mechanical, and functional levels.

Tissue-level drug-induced exacerbation of cardiotoxicity.

The ability to detect drug-induced exacerbation of cardiotoxicity is an unmet need in drug development to address safety concerns for patients with pre-existing cardiovascular conditions, as CVD is a common comorbidity of major diseases.[35] Cardiac infarct organoids provide a tissue-level model to evaluate drug-induced cardiotoxicity and/or exacerbation of heart failure and supports the efforts to study cardiac pathophysiology in the emerging field of cardio-oncology.[70,71] Previous research has shown that hiPSC-CMs from breast cancer patients with chemotherapy-induced cardiotoxicity were more sensitive to doxorubicin (DOX), a known cardiotoxic anticancer medication, than breast cancer patients without chemotherapy-induced cardiotoxicity, suggesting a genetic basis for DOX-based cardiotoxicity.[21] With a non-genetic basis for our disease model induction, we hypothesized that infarct organoids can be used as a tissue-level model to study a non-genetic basis for drug-induced exacerbation of cardiotoxicity in vitro that mimics the clinical observation of worsening heart failure of anthracycline-treated cancer patients with pre-existing cardiovascular risk.[72]

As a control, we performed 2D studies using hiPSC-CMs with DOX to evaluate the combined effects of an in vitro infarction protocol and DOX on hiPSC-CMs. Hypoxic culture (1%) with 1 μM NE in organoid media for 2 days prior to the 2 days DOX treatment caused an exacerbation of DOX-induced reduction in viability and reduction in contractile

structures/organization (Fig. S13a–S13c). Nearly ~100% cell death was found for hiPSC-CMs after 4 days of the same hypoxic culture using hiPSC-CM media (with galactose, but no glucose, similar media to the one used in the previous 2D hiPSC-CM DOX studies[21]), which has been attributed to the lack of glucose in the hiPSC-CM media (Fig. S14a). In addition, extended culture of 2D hiPSC-CMs in organoid media (to mimic our prolonged organoid infarction protocol) led to a reduction of functional αSA+ cells (Fig. S14b). In contrast to the inherent difficulties of using 2D hiPSC-CM culture systems to model post-MI responses, human infarct organoids provide a robust, biomimetic 3D tissue-level context to evaluate the effects of DOX on the post-MI cardiac tissues. Application of DOX showed functional toxicity with a reduced IC_{50} of contraction amplitude in infarct organoids (~0.35 μM) compared to control organoids (~0.41 μM) (Fig. 7a). This was further supported by cessation of beating in infarct and control organoids at 1 μM and 50 μM, respectively (Fig. 7a). The observed detrimental effects of DOX on contractile function in both control and infarct organoids is consistent with the clinical data showing decreased contractile function (i.e., left ventricular ejection fraction) after anthracycline exposure.[73] The reduction in organoid contraction was supported by the TUNEL analysis that showed significantly increased apoptosis for infarct organoids at 1 μM (Fig. 7b). Furthermore, infarct organoids displayed a more severe disarray of sarcomeric structures across 3D space (i.e., exterior to interior) compared to control organoids with increasing dose of DOX, where αSA staining significantly decreases relative to vehicle control most notably at the interior of infarct organoids at 0.1 μM in contrast to control organoids (Fig. 7c, 7d, S15, Table S5), consistent with the decreased contraction amplitude at low doses in infarct organoids.

In addition to hiPSC-CM-specific changes, DOX exposure induced an increase in vimentin+ density at a lower dose in infarct organoids (0.1 μM) than in control organoids (1.0 μM) (Fig. 7e, 7f, Table S7), indicating a similar phenotype to DOX-induced cardiac fibrosis.[74] This is supported by the histopathological evidence of fibrosis in myocardial biopsies from children and adults with anthracycline cardiotoxicity.[75–77] Overall, the use of cardiac infarct organoids in cardiotoxicity screening demonstrated that pre-existing (hypoxic) cardiac injury exacerbates the cardiotoxicity of DOX, in line with worsening heart failure of anthracycline-treated cancer patients with pre-existing cardiovascular risk.[72] The worsened phenotype of infarct organoids in response to DOX was reasoned to be attributed to pre-existing oxidative stress in infarct organoids evidenced by the previously mentioned metabolic shifts, hypoxia staining, and increased DNA damage as marked by TUNEL in the middle of infarct organoids in combination with the reported differential effect of DOX on different metabolic/oxidative states.[21] Our results demonstrated that human cardiac organoids allowed for the recapitulation of 3D tissue-level responses, including cardiac and fibrotic effects, to drug-induced/exacerbated cardiotoxicity.[70,78]

Discussion

By leveraging nutrient diffusion gradients in 3D microtissues, we developed a human cardiac organoid disease model that recapitulates major hallmarks of the acute post-MI cardiac state at a transcriptomic, structural and functional level. While human organoids have been widely used to study genetic factor-caused diseases, we demonstrated the use of tissue engineering principles (i.e., nutrient transport) to design an in vitro organotypic

disease model of CVD with non-genetic upstream pathological stimuli. It is our belief that the focus on upstream pathological stimuli allowed for the recapitulation of major downstream hallmarks of the human post-MI myocardium. While organoids have traditionally been prepared with embryoid bodies, this study demonstrated that the self-assembly of tissue-specific cell types provides a powerful alternative to prepare organoids with tissue-mimetic transcriptome, structure and function.[79] Through the integration of robust infarct organoid fabrication and imaging-based function analysis, we also established a method amenable for tissue-level heart failure drug testing and screening of drug-induced/exacerbated cardiotoxicity. As demonstrated with JQ1 and doxorubicin, this provides a strategy to investigate primary and secondary effects (e.g., how cellular changes effect tissue-level function) of drug treatments in the context of a 3D, multicellular organotypic model.

One limitation of the model is that not every aspect of heart failure can be mimicked with the current infarct organoids (e.g., lack of inflammatory cells, use of immature hiPSC-CMs).[80] However, the transcriptome- to function-level changes provided a multi-dimensional validation that illustrates the extent to which infarct organoids model responses of human cardiac tissue after infarction, consistent with the demonstrated feasibility of using iPSC-based systems to model diseases across many adult tissue types, including the heart.[3,5,18,19] Immune/inflammatory cell types are known to play a role in the early post-MI response and are thought to contribute to the activation of the subsequent fibrotic response.[80] Notably, the immune system-related terms seen in PCA analysis of infarct organoids and the occurrence of fibrotic response without the inclusion of immune cell types in the organoids gave evidence for the future use of our system to investigate how immune/inflammatory components affect the “cardiac tissue half” (e.g., cell-adhesion molecules, chemokines) of the immune-stromal interactions and may help to distinguish the level of contribution of cell types to myocardial fibrosis, for example. With limited in situ access to human cardiac tissues[32], human cardiac infarct organoids lay the groundwork for personalized models in precision cardiovascular medicine for future investigation into the genetic contributions to patients’ tissue-level response to myocardial infarction.[20,81,82]

Methods

Oxygen diffusion mathematical modeling.

A computational finite element model of nutrient (i.e., oxygen) diffusion and transport was developed to provide oxygen concentration profiles within cardiac spheroids (cardiomyocyte-only) based on Fick’s Second Law of Diffusion to serve as a general guiding design principle to support the organoid infarction protocol rationale. Given the developmental similarities between hiPSC-CMs and neonatal rat cardiomyocytes[83], neonatal cardiomyocyte metabolic data was used according to the detailed oxygen consumption work of Brown and others.[45] Specifically, the oxygen diffusivity value ($D_{Ox} = 3.0 \times 10^{-6}$ cm^2/s) and cardiomyocyte specific consumption rate constants for oxygen ($V_{max} = 5.44 \times 10^{-8}$ nmol/cell/s and $K_m = 3.79$ nmol/ml) were derived from Brown and others.[45] Next, the concentration-dependent nutrient consumption rate of the cardiomyocytes was modeled by the Michaelis-Menten equation $R = \rho_c \frac{V_{max}[C]}{K_m + [C]}$, where ρ_c represents spheroid cell density,

V_{max} maximum rate at high substrate concentration, and K_m Michaelis-Menten constant. Physiological (20%) and hypoxic (10%) culture conditions were accounted for in the boundary conditions of the model. In a spherical coordinate system, the internal oxygen concentration profile is governed by the equation $\frac{D}{r^2}\frac{\partial}{\partial r}\left(r^2\frac{\partial C}{\partial r}\right) - R = 0$, where C represents nutrient concentration, r radial distance from spheroid center, D nutrient diffusivity, and R nutrient consumption rate. Upon compiling all of the relevant equations, the finite element model was numerically solved by the software COMSOL Multiphysics, from which the internal oxygen concentration profiles were determined in simulated cardiomyocyte spheroids. In evaluating the finite element model, the semi-circular concentration profiles obtained by solving the finite element model on COMSOL were reformatted into line graphs that showed the change in oxygen levels based on radial position from the spheroid center. These plots were then assessed for trends that indicated the effects of external oxygen concentration on the internal oxygen distributions within the cardiac spheroid.

Cell culture.

Human induced pluripotent stem cell-derived cardiomyocytes (hiPSC-CMs) (iCell Cardiomyocytes, Cellular Dynamics International-CDI, Madison, WI, USA) were cultured according to the manufacturer's protocol. iCell Cardiomyocytes iPSC donor 01434 (i.e. Donor A) were used for all experiments and iCell Cardiomyocytes iPSC donor 11713 were used where notated as Donor B. Briefly, hiPSC-derived cardiomyocytes were plated on 0.1% gelatin coated 6-well plates in iCell Cardiomyocyte Plating Medium (CDI) at a density of about 3×10^5 to 4.0×10^5 cells/well and incubated at 37 °C in 5% CO_2 for 4 days. Two days after plating, the plating medium was removed and replaced with 4 mL of iCell Cardiomyocytes Maintenance Medium (CDI). After 4 days of monolayer pre-culture, cells were detached using trypLE Express (Gibco Life Technologies, Grand Island, NY) and prepared for spheroid/organoid fabrication. For 2D hiPSC-CM doxorubicin experiments, cells were plated in 96 well plates (20×10^3 cells/well) and let culture for 2 days in iCell Cardiomyocytes Maintenance Medium (CDI) before starting treatment. Human cardiac ventricular fibroblasts (FBs) (CC-2904, Lot#: 0000401462, Lonza, Basel, Switzerland) were cultured in FGM-2 media (Lonza) were used at passage 3-5 for spheroid/organoid fabrication. Human umbilical vein endothelial cells (HUVECs) (C2519A, Lot#: 0000471466, Lonza) were cultured in EGM-3 media (Lonza) and were used at passage 2-4 for organoid fabrication. Human adipose-derived stem cells (hADSCs) (PT-5006, Lot#: 0000410257, Lonza) were cultured in low glucose Dulbecco's modified Eagle's medium with 10% fetal bovine serum (FBS) and 1% penicillin-streptomycin, 1% glutamine and 1% antimycin (Gibco Life Technologies, Grand Island, NY). hADSCs were used at passage 5-7 for organoid fabrication. For 2D hiPSC-CM doxorubicin experiments, CyQUANT XTT Cell Viability Assay (X12223, Thermo) was used to measure differences in cell viability between conditions.

Organoid and spheroid fabrication.

Organoid fabrication is described in our previous publication.[43] Briefly, non-adhesive agarose hydrogel molds were used as microtissue fabrication molds made from commercial master micro-molds from Microtissues, Inc (Providence, RI), where each agarose mold

contains 35 micromold recesses. Organoid cell suspensions were comprised of 50% hiPSC-CMs and 50% non-myocyte (at a 4:2:1 ratio of FBs, HUVECs, hADSCs, respectively) in media for a final concentration of ~2.0 x 10^6 cells/ml. Monocellular spheroids (hiPSC-CM only, cardiac FB only) were fabricated using a concentration of ~2.0 x 10^6 cells/ml. To make microtissues (organoid or spheroid) of ~150 μm radius, approximately 75 μl of the organoid or spheroid cell suspension (~150,000 cells) was pipetted into each agarose mold. After the cells settled into the micromold recesses of the mold (15 min), additional media was added to submerge the molds in a 12-well plate and exchanged every 2 days for the length of the experiment. Day 0 (D0) of the experiment was marked after 4 days of organoid self-assembly, after which the control or organoid infarction protocol was initiated for 10 additional days (D0 to D10). Culture media for cardiac organoids was comprised of a ratiometric combination of cell-specific media reflecting the starting cell ratio of the organoid. In organoid media, the CM-specific component was defined as glucose-containing F12/DMEM media with 10% FBS, 1% glutamine, and 1% non-essential amino acids (Gibco). In this paper, the “organoid” term only refers to microtissues made with >2 input cell types, whereas “spheroid” refers to monocellular microtissues.

Cardiac organoid infarction protocol.

For the cardiac organoid infarction protocol, microtissues (~150 μm radius on D0) were placed in a hypoxia chamber (ProOx Model 110, BioSpherix, Parish, NY) within the incubator at 10% O_2 with 1 μM of norepinephrine (NE, A7257, Sigma) for 10 days. Media was changed (with NE) every 2 days for the length of the experiment. The L-Lactate Assay Kit (Colorimetric) (ab65331, Abcam, Cambridge, UK) was used to measure L-lactate levels in the media of D10 control and infarct organoids.

Contraction analysis of beating spheroids.

Videos of spontaneously beating spheroids from each group were recorded immediately out of the incubator (to reduce temperature induced changes in beating) for each condition using a Carl Zeiss Axiovert A1 Inverted Microscope and Zen 2011 software (Zeiss, Göttingen, Germany). Threshold edge-detecting in ImageJ software (NIH - US National Institutes of Health) was used on high contrast spheroid picture series and graphed to realize beating profiles of fractional area change, from which contraction amplitude was calculated. Contraction amplitudes were calculated as the percent change in fractional area change amplitude between contraction and relaxation. Beat rate was calculated as the number of beats per second.

RNA sequencing.

Total RNA was isolated one day after last media change (D11) according to the kit and protocol of an Omega bio-tek E.Z.N.A. Total RNA kit I (Omega bio-tek, Norcross, GA) with the addition of the Homogenizer Columns (Omega bio-tek) during the homogenization step for organoids. For each group, 30-35 organoids were used for RNA isolation. To prepare RNA-seq libraries, the TruSeq RNA Sample Prep Kit (Illumina, San Diego, CA, USA) was utilized; 100–200 ng of total input RNA was used in accordance with the manufacturer’s protocol. High throughput sequencing (HTS) was performed using an Illumina HiSeq2000 with each mRNA library sequenced to a minimum depth of ~50 million reads. A single end

50 cycle sequencing strategy was employed. Data were subjected to Illumina quality control (QC) procedures (>80% of the data yielded a Phred score of 30). RNA-seq data has been submitted to the NCBI Gene Expression Omnibus under accession numbers GSE113871, GSE115031.

Secondary analyses was carried out on an OnRamp Bioinformatics Genomics Research Platform as previously described (OnRamp Bioinformatics, San Diego, CA, USA).[84] OnRamp's Advanced Genomics Analysis Engine utilizes an automated RNA-seq workflow to process data, including (1) FastQC to perform data validation and quality control; (2) CutAdapt[85] to trim and filter adapter sequences, primers, poly-A tails and other unwanted sequences; (3) TopHat2[86] to align mRNA-seq reads to hg19 genome using the ultra-high-throughput splice aware short read aligner Bowtie2[87]; (4) HTSeq[88] to establish counts which represent the number of reads for each transcript; and (5) DESeq2[89] to perform DE analysis, which enabled the inference of differential signals with robust statistical power. Transcript count data from DESeq2 analysis of the samples were sorted according to their adjusted *p*-value (or *q*-value), which is the smallest false discovery rate (FDR) at which a transcript is called significant. FDR is the expected fraction of false positive tests among significant tests and was calculated using the Benjamini-Hochberg multiple testing adjustment procedure. Advaita Bio's iPathwayGuide was used to perform further characterization, including a summary of differential expressed (DE) genes, gene ontology, and pathway analysis for genes with at least 0.2 fold change in positive or negative direction and *q*-value of <0.4.[90]

Transcriptional comparative analysis.

Previously published transcriptomic datasets were obtained through the Gene Expression Omnibus (GEO). Microarray data from a large human heart failure study[91] (GSE5406, n = 16 "nonfailing" and 108 "ischemic" samples), a time-course mouse myocardial infarction study[29] (GSE775, n = 3 "lv-control", 3 "MI_ilv-below MI ligation site", and 3 "MI_nilv-above MI ligation site" samples), and a time-course porcine myocardial infarction study[28] (GSE34569, n = 3 "sham-operated", 3 "infarct core", and 3 "remote" samples) were analyzed using the interactive GEO web tool (limma-based), GEO2R, to obtain summary files of genes ordered by statistical significance.[92–94] Differentially expressed (DE) genes (based on $p < 0.05$) for Venn diagrams were obtained from comparisons of control vs infarct (organoids), nonfailing vs ischemic failing (human, GSE5406, due to its larger sample size), control vs MI infarct zone at 1 wk (mouse), sham vs MI infarct at 1 wk (porcine), and nonfailing vs ischemic cardiomyopathy failing (human, GSE46224). For Venn diagram comparison across datasets, DE genes were directly compared using gene symbols for common genes between studies (excluding nonoverlapping genes from platform differences, such as RNA-seq vs microarray chip) using Venny and graphed using VennDis.[95,96] Gene ontology (biological process) of the overlapping DE genes was characterized using the ToppFun component of the ToppGene suite.[97] RNA-seq datasets were obtained from GEO from a public human heart failure study[98] (GSE46224, n = 8 "ischemic cardiomyopathy (ICM)" and 8 "nonfailing" samples) and a mouse 2 wk myocardial infarction study[99] (GSE52313, n = 4 "sham" and 4 "MI" samples). Before merging gene lists for principal component analysis (PCA), organoid, human, and mouse RNA-seq data were normalized to the size of the library through the R package DESeq2 estimateSizeFactors function and

labeled with gene symbols. For human RNA-seq data, starting counts were calculated based on the supplied RPKM and read counts/mapping details for nonfailing and ICM samples from the associated publication.[98] After merging normalized organoid, human, and mouse RNA-seq data, the resulting 4,765 shared genes were $\log_2$-transformed followed by quantile normalization using the normalize.quantiles function in the preprocessCore package. PCA was then performed using the prcomp function in R and plotted as scatter plots (using jitter) with basic plotting tools in R. Principal component gene loadings were used as rankings for genes in gene set enrichment analysis (GSEA) with the gene ontology c5.all.v6.1.symbols.gmt file, run with default settings.[100] GSEA terms were considered significant with a normalized p-value (NOM p-value) less than 0.05 and a false discovery rate (FDR) less than 0.25. Supplemental PCA using normalized mouse heart sham samples from another study (GSE96561) was performed after merging data into heart failure data, resulting in 4,244 shared genes.[69]

The “metabolic pathways” gene set was based on KEGG pathway “map01100”, a large pathway term including several metabolic modules, and was constructed based on the DE genes found in the organoid RNAseq data for a total of 242 genes. Given the lack of cardiac fibrosis pathway term and subjective nature of fibrosis in the heart, the fibrosis-related gene set was constructed based on the “extracellular matrix organization” GO term in addition to a “greedy”-based selection that incorporated common factors in fibrosis and (myo)fibroblast-related genes for a total of 349 genes. The calcium signaling-related gene set was defined as the genes contained in the “calcium signaling pathway” KEGG term 4020 for a total of 182 genes. Cardiac organoid RNA-seq and mouse 1 wk MI microarray (GSE775) were first intersected to isolate for common genes across platforms and then merged again with the filter gene sets, resulting in 208 fibrosis-related genes in organoids and mouse and 121 calcium-related genes in organoids and mouse. Heatmaps of fibrosis-related gene sets in organoids and mouse data were constructed separately using the pheatmap package in R with hierarchical clustering of samples (columns) with category-ordered genes (rows). Heatmaps of metabolic pathways and calcium handling-related gene sets in organoids and mouse data were constructed in like manner but with row order based on the organoid log-fold change. Assembled and filtered gene set lists can be found in Table S2, S3, and S4. Representative genes were expressed as Transcripts Per Million (TPM).

Fluorescent imaging and analysis.

Freshly collected organoids were flash frozen in Tissue-Tek OCT compound (Sakura, Torrance, CA). Embedded spheroids were cryosectioned into 7 μm thickness layers onto glass slides for immunofluorescence staining. The sections were fixed with pre-cooled acetone (−20 °C) for 10 min. After washing (2 times at 5 min) in PBS with 0.1% Triton X-100 (PBST) (Sigma), blocking buffer was made with 10% serum corresponding to host species of secondary antibody in PBST and added to sections for 1 hr at room temperature. Sections were incubated with primary antibody diluted in PBST (1:200) overnight at 4 °C or 2 hrs at room temperature: mouse anti-alpha smooth muscle actin (catalog# A5228, clone 1A4, lot# 056M4828V, Sigma), mouse anti-alpha sarcomeric actinin (catalog# ab9465, clone EA-53, lot# GR3174517-4, Abcam), rabbit anti-collagen type I (catalog# ab34710, polyclonal, lot# GR248854-2, Abcam), rabbit anti-vimentin (catalog# ab92547, clone

EPR3776, lot# GR3258719-6, Abcam), and rabbit anti-von Willebrand factor (catalog# ab6994, polyclonal, lot# GR3180938-1, Abcam). After washing in PBST (2 times at 5 min), sections were incubated with complement secondary antibodies or conjugated primary antibodies diluted in PBST for 1 hr at room temperature: Alexa Fluor 488 phalloidin (catalog# A12379, lot# 2026144, Thermo), goat anti-mouse Alexa Fluor 546 (catalog# A1103, polyclonal, lot# 2026144, Thermo), goat anti-rabbit Alexa Fluor 647 (catalog# 111-605-144, polyclonal, lot# 113514, Jackson ImmunoResearch, West Grove, PA). After washing in PBST (2 times at 5 min), nuclei were counterstained with DAPI (Molecular Probes/Invitrogen, Eugene, OR) diluted in PBST for 15 min at room temperature. Following the final wash procedure (PBST, 2 times at 5 min), glass cover slips were added using Fluoro-Gel (Electron Microscopy Sciences, Hatfield, PA) and stored in 4 °C until imaging. TCS SP5 AOBS laser scanning confocal microscope (Leica Microsystems, Inc., Exton, PA) was used for imaging of microtissue sections where z-stacks of 3-4 μm thickness with 0.5-1 μm step sizes were used. Stained 2D hiPSC-CMs in 96-well plates were imaged with a Carl Zeiss Axiovert A1 Inverted Microscope and Zen 2011 software (Zeiss). Vimentin radial density was calculated using the Radial Profile ImageJ plugin and normalized to radius equal to 1 to provide radial density profile plots of normalized integrated intensities. Normalized fibrillar alpha smooth muscle actin area was calculated by dividing the area covered by positively-stained fibrillar structures (as opposed to blotchy or diffuse staining) by the total area of alpha smooth muscle actin-positive staining followed by dividing by the total organoid cross-sectional area. These results were then normalized to the average of the control organoid results. Each analysis consisted of high resolution images at 400X total magnification of cross sections of different organoids.

The Roche In Situ Cell Death Detection Kit (Sigma) was used for to visualize apoptotic cells in frozen sections of cardiac organoids based on the Roche protocol. Briefly, cardiac organoid frozen sections were fixed with 4% paraformaldehyde in PBS for 20 min at room temperature. Following washing in PBS for 30 minutes, samples were incubated in a permeabilization solution (0.1% Triton X-100 and 0.1% sodium citrate in PBS) for 2 minutes on ice. Then 50 μl of the TUNEL reaction mixture were added to samples and incubated at 37 °C for 1 hr. After washing in PBS (2 times at 5 min), nuclei were counterstained with DAPI (Molecular Probes/Invitrogen) diluted in PBS for 15 min at ambient temperature. Following the final wash procedure (PBS, 2 times at 5 min), glass cover slips were added to the slides using Fluoro-Gel (Electron Microscopy Sciences). TCS SP5 AOBS laser scanning confocal microscope (Leica Microsystems) was used for imaging of microtissue sections where z-stacks of 3-4 μm thickness with 0.5-1 μm step sizes were used.

Hypoxia imaging was performed using the Image-iT Green Hypoxia kit. A working concentration of 4 μm of the Image-iT Hypoxia Reagent was used in the media of control and infarct organoids for overnight culture in their respective conditions. After 24hrs, organoids were live-imaged using a TCS SP5 AOBS laser scanning confocal microscope (Leica Microsystems). Images were taken from ~30-40 μm under the surface of the organoid. The resulting hypoxia stain was quantified using radial density calculated using the Radial Profile ImageJ plugin to provide radial density profile plots of normalized integrated intensities.

NADH autofluorescence imaging of live cardiac organoids was performed in media at 37 °C within 1 hour of removal from culture conditions using an Olympus FV1200 laser scanning two-photon excitation fluorescence microscope, which is equipped with a tunable ultrafast laser (Maitai, Newport) and two GaAsP PMTs. The excitation wavelength was tuned to 730 nm for autofluorescence imaging and a filter separated fluorescence with a passing band of violet (420-460 nm), which has been primarily attributed to NAD(P)H fluorescence.[101] For each group (i.e., control, infarct, and dead organoids), background mean grey values were first subtracted from the mean grey value of the sample area NADH autofluorescence (30-40 μm below organoid surface) to give separate "NADH values" per sample. The NADH index was then calculated as each sample "NADH value" divided by the average of the dead organoid sample "NADH values."

Seahorse mitochondrial stress test.

The bioenergetics of organoids was assessed using the Seahorse XF Cell Mitochondrial Stress Test (Agilent) designed for measuring 3D spheroids.[102] Cell-Tak (22 μg/mL, pH 6.5-8, Corning, Cat# 354241) was coated in wells of a Seahorse XFe96 spheroid microplate (Agilent, Cat# 102959-100) at 37°C for 20 minutes. Cell-Tak was neutralized with DI H_2O and wells were rinsed twice with DI H_2O, dried and stored at 4°C. Single organoids were transferred into wells containing organoid media and allowed to attach overnight at 37°C in their respective conditions. The following day, the media was replaced with low phosphate DMEM buffer and warmed in a 37 °C non-CO_2 incubator. The day before the test, the sensor cartridge was placed in the calibration buffer provided by Seahorse Agilent. Oxygen consumption rates (OCR) and extracellular acidification rates (ECAR) were measured before and after administration of oligomycin (2 μM, Sigma), carbonyl cyanide-p-trifluoromethoxyphenylhydrazone (FCCP) (1 μM, Sigma) and Rotenone/Antimycin A (2 μM, Sigma). The injection ports of the sensor plate were filled with 25 μl of compounds or vehicle diluted in DMEM buffer. The sensor plate was placed into the XF-96e instrument for calibration. After calibration, the calibration fluid plate was removed, and the cell plate was loaded for analysis. The measurement protocol was set to 3 min mixes and 3 min measurements. There were 12 rate measurements post injections (basal levels, Oligomycin, FCCP, and Antimycin/Rotenone), and each injection had 6 measurement cycles, while Oligomycin had 9 measurement cycles. Images of organoids in microplates were taken using 4X magnification and area of each organoid was analyzed using an IncuCyte live-cell analyzer (Sartorius).

Mechanical testing using micropipette aspiration.

A micropipette aspiration was performed in media similarly to previous studies using a custom-built fluid reservoir to generate a fixed pressure of 40 cmH_20 (~3.9 kPa) in pulled micropipette to apply the suction force on test organoids.[61,103] Validation and stability of pressure changes were confirmed using an in-line 5 kPa 2-port pressure transducer with ~1 Pa sensitivity (Honeywell, Morristown, NJ). Micropipettes were pulled to a final inner diameter of approximately 70-80 μm. Prior to and during testing, organoids were soaked in a 30 mM solution of 2,3-butanedione monoxime (BDM) (Sigma) in media for 5-10 min to eliminate contractions to reduce the effect of contractile status on tissue stiffness. Pressure was applied to the organoid surface and pictures were recorded until reaching equilibrium

deformation (~5 min). Under the homogeneous half-space model assumptions[61], the change in length (L) from pre-deformation to equilibrium deformation was used to calculate the elastic modulus according the previously established relationship: $E = \frac{3a\Delta p}{2\pi L}\Phi(\eta)$, where E is elastic modulus, a is the inner micropipette radius, Δp is the applied pressure, Φ() is the wall function, and η is the wall parameter, where Φ() and η are dependent on the geometry of the micropipette tip.[103,104]

Development of customized two-photon scanned light-sheet microscope for calcium transient imaging.

The customized two-photon scanned light-sheet microscope (2PLSM) scans the near-IR laser beam laterally to create a thin excitation light-sheet in a specimen and simultaneously collects two-photon excitation fluorescence images with a high speed camera. This microscope has taken advantage of the deep penetration depth brought by the two-photon excitation and the fast imaging speed enabled by the light-sheet imaging with the high-speed camera. As shown in Figure S6, the 2PLSM comprises two main optical paths: one for generating two-photon excitation light-sheet and the other for image collection; two responsible microscope objectives are used for illumination and imaging respectively and are aligned orthogonally to each other. For generating the light-sheet, the laser beam from the tunable (690-1080 nm) femtosecond laser (TSUNAMI, Newport, CA) is focused by the first achromatic lens (L1, AC254-75-B-ML, Thorlabs, NJ) and then collimated by the second achromatic lens (L2, AC508-75-B-ML, Thorlabs, NJ). A MEMS (Micro-electro-mechanical system) scan mirror (gold coated integrated module, mirror diameter 1200 μm, Mirrorcle, CA) is placed near the focus of the first lens and scans the beam two-dimensionally (Fig. S7). The surface of the MEMS mirror is imaged onto the back focal plane of the illumination objective (OBJ 1, CFI Plan Fluor 10X, Water dipping, NA 0.30, WD 3.5mm, Nikon Instruments, NY) so that the horizontal scan created the light-sheet extended in the XY-plane and the vertical scan positions the light-sheet in the Z-direction. The two-photon excitation fluorescence signal is collected by the imaging objective (OBJ 2, 40X Nikon CFI APO NIR, water dipping, NA 0.80, WD 3.5 mm, Nikon Instruments, NY) and a camera lens (EF 28-135mm f/3.5-5.6 IS USM, Canon, Japan). Calcium events, as reflected by the fluorescence change of the calcium indicator GCaMP6, were recorded by a sCMOS camera (Zyla 4.2, Andor technology, UK) with a band-pass filter (FF03-525/50-25, 500-550 nm, Semrock, NY). The maximum frame rate of the sCMOS was 100 frames/second at the full frame size (2048 x 2048 pixels). The laser beam was scanned through the selected illumination plane at least twice during every exposure period to ensure the uniformity of the illumination. A piezo electric objective z-drive (P-725 PIFOC, Physik Instrumente, MA) was used to keep the illumination plane in the focus of the imaging objective. Both the MEMS scanning and the z-drive movement were controlled by customized software written in LabVIEW (National Instrument, TX).

To minimize fluorescence drift and avoid microtissue diffusion limitations of dye-based fluorescent tags (e.g., Fluo-4), hiPSC-CMs were infected overnight (~16 hrs) with GCaMP6 adenovirus (gift from Dr. Martin Morad) the day before organoid fabrication. Imaging was performed at room temperature within 1 hour of removal from culture conditions on organoids in non-adhesive, clear agarose molds submersed in calcium buffer from Life

Technologies's Fluo-4 Direct Calcium Assay Kit (Life Technologies, Carlsbad, CA). The two-photon excitation light-sheet imaging was performed using Micro-manager (NIH) to capture the calcium dynamics of the micro-tissue.[105] With an image size of 512 × 512 pixels (202 x 202 μm), a 60-sec video (3000 frames) at 50 frames/sec was taken for the selected plane of each organoid at >50 μm below organoid surface. ImageJ (NIH) and home developed Matlab program were applied for image processing and data analysis. Each video was displayed in ImageJ and manually circled cell-sized ROIs to represent individual fluorescing cardiomyocytes and the mean value of the ROI was plotted over time representing the calcium transient. Calcium transient amplitude ($\Delta F/F_0$) was calculated as the difference of peak and baseline calcium fluorescence (ΔF) divided by the baseline fluorescence level (F_0).

Drug testing.

For targeted heart failure drug testing, 10 nM of JQ1 (SML1524, Sigma) was added to the media on D0 every 2 days for infarct organoids for the length of the experiment (10 days). For 2D hiPSC-CM experiments, cells were plated for 2 days on gelatin-coated 96 well plates (20,000 cells per well) in iCell Cardiomyocytes Maintenance Medium (CDI), changed to organoid media for 2 days in control or "2D infarction" conditions (1% O_2 with 1 μM NE), and then doxorubicin doses were added to culture for 2 more days. For detection of exacerbation of drug-induced cardiotoxicity in cardiac organoids, a range (0-50 μM) of doxorubicin (D1515, Sigma) was added to media on D10 and cultured for 2 days in control or infarct conditions.

Statistics analysis.

Differences between experimental groups were analyzed through Excel and GraphPad Prism 7.0 statistical tools. Sample distribution was assumed normal with equal variance and Student's t-test, one-way ANOVA with Bonferroni-corrected t-test post-hoc, and two-way ANOVA with Tukey post-hoc analysis with $p<0.05$ were considered as significantly different. Sample sizes of biologically independent samples per group are notated in the figure legends as n = X per group / Y independent experiments, where applicable.

Reporting summary.

Further information on research design is available in the Nature Research Reporting Summary linked to this article.

Data availability.

The main data supporting the results in this study are available within the paper and its Supplementary Information. The raw and analyzed datasets generated during the study are available from the corresponding authors on reasonable request. RNA-seq data are available from the NCBI Gene Expression Omnibus, under the accession numbers GSE113871 and GSE115031.

Code availability.

The code that support the findings of this study (to control the custom built two-photon scanned light-sheet microscope written in LabVIEW) are available from the corresponding author upon reasonable request.

Supplementary Material

Refer to Web version on PubMed Central for supplementary material.

Acknowledgments

The authors would like to acknowledge Willian da Silveira for insight into microarray/RNA-seq/GSEA analysis and the laboratory of Dr. Martin Morad for help with GCaMP6 labeling. The work was supported by the National Institutes of Health (R01 HL133308, 8P20 GM103444, U54 GM104941), National Institute of General Medical Sciences (P20GM-103499), startup funds from Clemson University, the National Science Foundation (NSF - EPS-0903795, 1539034), the NIH Cardiovascular Training Grant (T32 HL007260), SCTR Institute CTSA NIH/NCATS (UL1TR001450), and US Department of Veterans Affairs Merit Review (I01 BX002327). This project was also supported by NIH grants, R03 DE018741, R01 DE021134 and P20GM121342, to H.Y. This study used the services of the Morphology, Imaging, and Instrumentation Core, which is supported by NIH-NIGMS P30 GM103342 to the South Carolina COBRE for Developmentally Based Cardiovascular Diseases and was supported in part by the Genomics Shared Resource, Hollings Cancer Center, Medical University of South Carolina (P30 CA138313), and the Bioenergetics Profiling Core, which is supported by the COBRE in Redox, Oxidant Balance, and Stress Signaling (NIH/NIGMS P20 GM103542). This study also supported by South Carolina Translational Research Improving Musculoskeletal Health (P20 GM121342).

References

1. Chamberlain SJ Disease modelling using human iPSCs. Hum. Mol. Genet 25, R173–R181, doi:10.1093/hmg/ddw209 (2016). [PubMed: 27493026]
2. Inoue H, Nagata N, Kurokawa H & Yamanaka S iPS cells: a game changer for future medicine. EMBO J. 33, 409–417, doi:10.1002/embj.201387098 (2014). [PubMed: 24500035]
3. Clevers H Modeling Development and Disease with Organoids. Cell 165, 1586–1597, doi:10.1016/j.cell.2016.05.082 (2016). [PubMed: 27315476]
4. Fatehullah A, Tan SH & Barker N Organoids as an in vitro model of human development and disease. Nat. Cell Biol. 18, 246–254, doi:10.1038/ncb3312 (2016). [PubMed: 26911908]
5. Lancaster MA & Knoblich JA Organogenesis in a dish: modeling development and disease using organoid technologies. Science 345, 1247125, doi:10.1126/science.1247125 (2014). [PubMed: 25035496]
6. Driehuis E & Clevers H CRISPR/Cas 9 genome editing and its applications in organoids. Am. J. Physiol. Gastrointest. Liver Physiol. 312, G257–G265, doi:10.1152/ajpgi.00410.2016 (2017). [PubMed: 28126704]
7. Nie J & Hashino E Organoid technologies meet genome engineering. EMBO Rep 18, 367–376, doi:10.15252/embr.201643732 (2017). [PubMed: 28202491]
8. Di Lullo E & Kriegstein AR The use of brain organoids to investigate neural development and disease. Nat. Rev. Neurosci 18, 573–584, doi:10.1038/nrn.2017.107 (2017). [PubMed: 28878372]
9. Drost J & Clevers H Organoids in cancer research. Nat. Rev. Cancer 18, 407–418, doi:10.1038/s41568-018-0007-6 (2018). [PubMed: 29692415]
10. Noordhoek J, Gulmans V, van der Ent K & Beekman JM Intestinal organoids and personalized medicine in cystic fibrosis: a successful patient-oriented research collaboration. Curr. Opin. Pulm. Med 22, 610–616, doi:10.1097/MCP.0000000000000315 (2016). [PubMed: 27635627]
11. Nantasanti S, de Bruin A, Rothuizen J, Penning LC & Schotanus BA Concise Review: Organoids Are a Powerful Tool for the Study of Liver Disease and Personalized Treatment Design in Humans and Animals. Stem Cells Transl Med 5, 325–330, doi:10.5966/sctm.2015-0152 (2016). [PubMed: 26798060]

12. Benjamin EJ et al. Heart Disease and Stroke Statistics-2017 Update: A Report From the American Heart Association. Circulation 135, e146–e603, doi:10.1161/CIR.0000000000000485 (2017). [PubMed: 28122885]
13. Tiburcy M et al. Defined Engineered Human Myocardium With Advanced Maturation for Applications in Heart Failure Modeling and Repair. Circulation 135, 1832–1847, doi:10.1161/CIRCULATIONAHA.116.024145 (2017). [PubMed: 28167635]
14. Zhang D et al. Tissue-engineered cardiac patch for advanced functional maturation of human ESC-derived cardiomyocytes. Biomaterials 34, 5813–5820, doi:10.1016/j.biomaterials.2013.04.026 (2013). [PubMed: 23642535]
15. Giacomelli E et al. Three-dimensional cardiac microtissues composed of cardiomyocytes and endothelial cells co-differentiated from human pluripotent stem cells. Development 144, 1008–1017, doi:10.1242/dev.143438 (2017). [PubMed: 28279973]
16. Ulmer BM et al. Contractile Work Contributes to Maturation of Energy Metabolism in hiPSC-Derived Cardiomyocytes. Stem Cell Rep. 10, 834–847, doi:10.1016/j.stemcr.2018.01.039 (2018).
17. Mills RJ et al. Functional screening in human cardiac organoids reveals a metabolic mechanism for cardiomyocyte cell cycle arrest. Proc. Natl. Acad. Sci. U. S. A 114, E8372–E8381, doi:10.1073/pnas.1707316114 (2017). [PubMed: 28916735]
18. Liang P et al. Drug screening using a library of human induced pluripotent stem cell-derived cardiomyocytes reveals disease-specific patterns of cardiotoxicity. Circulation 127, 1677–1691, doi:10.1161/CIRCULATIONAHA.113.001883 (2013). [PubMed: 23519760]
19. Dell'Era P et al. Cardiac disease modeling using induced pluripotent stem cell-derived human cardiomyocytes. World J. Stem Cells 7, 329–342, doi:10.4252/wjsc.v7.i2.329 (2015). [PubMed: 25815118]
20. Matsa E et al. Transcriptome Profiling of Patient-Specific Human iPSC-Cardiomyocytes Predicts Individual Drug Safety and Efficacy Responses In Vitro. Cell Stem Cell 19, 311–325, doi:10.1016/j.stem.2016.07.006 (2016). [PubMed: 27545504]
21. Burridge PW et al. Human induced pluripotent stem cell-derived cardiomyocytes recapitulate the predilection of breast cancer patients to doxorubicin-induced cardiotoxicity. Nat. Med 22, 547–556, doi:10.1038/nm.4087 (2016). [PubMed: 27089514]
22. Wang G et al. Modeling the mitochondrial cardiomyopathy of Barth syndrome with induced pluripotent stem cell and heart-on-chip technologies. Nat. Med 20, 616–623, doi:10.1038/nm.3545 (2014). [PubMed: 24813252]
23. Ma Z et al. Contractile deficits in engineered cardiac microtissues as a result of MYBPC3 deficiency and mechanical overload. Nat. Biomed. Eng, doi:10.1038/s41551-018-0280-4 (2018).
24. Yusuf SA 35-year journey to evidence-based medicine: a personal story. Eur. Heart J. 36, 3460–3466, doi:10.1093/eurheartj/ehv566 (2015). [PubMed: 26586778]
25. Gheorghiade M et al. Developing New Treatments for Heart Failure: Focus on the Heart. Circ. Heart Fail. 9, doi:10.1161/CIRCHEARTFAILURE.115.002727 (2016).
26. Fine B & Vunjak-Novakovic G Shortcomings of Animal Models and the Rise of Engineered Human Cardiac Tissue. ACS Biomater. Sci. Eng. 3, 1884–1897, doi:10.1021/acsbiomaterials.6b00662 (2017).
27. Kaye DM & Krum H Drug discovery for heart failure: a new era or the end of the pipeline? Nat. Rev. Drug Discov. 6, 127–139, doi:10.1038/nrd2219 (2007). [PubMed: 17268484]
28. Prat-Vidal C et al. Identification of temporal and region-specific myocardial gene expression patterns in response to infarction in swine. PLoS One 8, e54785, doi:10.1371/journal.pone.0054785 (2013). [PubMed: 23372767]
29. Tarnavski O et al. Mouse cardiac surgery: comprehensive techniques for the generation of mouse models of human diseases and their application for genomic studies. Physiol. Genomics 16, 349–360, doi:10.1152/physiolgenomics.00041.2003 (2004). [PubMed: 14679301]
30. Chen T & Vunjak-Novakovic G Human Tissue-Engineered Model of Myocardial Ischemia-Reperfusion Injury. Tissue Eng Part A, doi:10.1089/ten.TEA.2018.0212 (2018).
31. Ugolini GS et al. Human cardiac fibroblasts adaptive responses to controlled combined mechanical strain and oxygen changes in vitro. Elife 6, doi:10.7554/eLife.22847 (2017).

32. Lowes BD et al. Serial gene expression profiling in the intact human heart. J. Heart Lung Transplant. 25, 579–588, doi:10.1016/j.healun.2006.01.006 (2006). [PubMed: 16678038]
33. Stevens JL & Baker TK The future of drug safety testing: expanding the view and narrowing the focus. Drug Discov. Today 14, 162–167, doi:10.1016/j.drudis.2008.11.009 (2009). [PubMed: 19100337]
34. Horvath P et al. Screening out irrelevant cell-based models of disease. Nat. Rev. Drug Discov. 15, 751–769, doi:10.1038/nrd.2016.175 (2016). [PubMed: 27616293]
35. Page RL 2nd, et al. Drugs That May Cause or Exacerbate Heart Failure: A Scientific Statement From the American Heart Association. Circulation 134, e32–69, doi:10.1161/CIR.0000000000000426 (2016). [PubMed: 27400984]
36. Nunes SS et al. Human Stem Cell-Derived Cardiac Model of Chronic Drug Exposure. ACS Biomaterials Science and Engineering (2016).
37. Occhetta P et al. A three-dimensional in vitro dynamic micro-tissue model of cardiac scar formation. Integr. Biol. (Camb.) 10, 174–183, doi:10.1039/c7ib00199a (2018). [PubMed: 29532839]
38. Sadeghi AH et al. Engineered 3D Cardiac Fibrotic Tissue to Study Fibrotic Remodeling. Adv Healthc Mater 6, doi:10.1002/adhm.201601434 (2017).
39. van Spreeuwel ACC et al. Mimicking Cardiac Fibrosis in a Dish: Fibroblast Density Rather than Collagen Density Weakens Cardiomyocyte Function. J. Cardiovasc. Transl. Res 10, 116–127, doi:10.1007/s12265-017-9737-1 (2017). [PubMed: 28281243]
40. Zhao H et al. Microengineered in vitro model of cardiac fibrosis through modulating myofibroblast mechanotransduction. Biofabrication 6, 045009, doi:10.1088/1758-5082/6/4/045009 (2014). [PubMed: 25378063]
41. Radisic M et al. Oxygen gradients correlate with cell density and cell viability in engineered cardiac tissue. Biotechnology and bioengineering 93, 332–343, doi:10.1002/bit.20722 (2006). [PubMed: 16270298]
42. Lymperopoulos A, Rengo G & Koch WJ Adrenergic nervous system in heart failure: pathophysiology and therapy. Circ. Res 113, 739–753, doi:10.1161/CIRCRESAHA.113.300308 (2013). [PubMed: 23989716]
43. Richards DJ et al. Inspiration from heart development: Biomimetic development of functional human cardiac organoids. Biomaterials 142, 112–123, doi:10.1016/j.biomaterials.2017.07.021 (2017). [PubMed: 28732246]
44. Frangogiannis NG Pathophysiology of Myocardial Infarction. Compr Physiol 5, 1841–1875, doi:10.1002/cphy.c150006 (2015). [PubMed: 26426469]
45. Brown DA et al. Analysis of oxygen transport in a diffusion-limited model of engineered heart tissue. Biotechnol. Bioeng 97, 962–975, doi:10.1002/bit.21295 (2007). [PubMed: 17195988]
46. Davis BH et al. Effects of myocardial infarction on the distribution and transport of nutrients and oxygen in porcine myocardium. Journal of biomechanical engineering 134, 101005, doi:10.1115/1.4007455 (2012). [PubMed: 23083196]
47. Semenza GL Hypoxia-inducible factor 1: regulator of mitochondrial metabolism and mediator of ischemic preconditioning. Biochim. Biophys. Acta 1813, 1263–1268, doi:10.1016/j.bbamcr.2010.08.006 (2011). [PubMed: 20732359]
48. Beeson CC, Beeson GC & Schnellmann RG A high-throughput respirometric assay for mitochondrial biogenesis and toxicity. Anal. Biochem 404, 75–81, doi:10.1016/j.ab.2010.04.040 (2010). [PubMed: 20465991]
49. Graham RM et al. A unique pathway of cardiac myocyte death caused by hypoxia-acidosis. J. Exp. Biol 207, 3189–3200, doi:10.1242/jeb.01109 (2004). [PubMed: 15299040]
50. Kligfield P, Horner H & Brachfeld N A model of graded ischemia in the isolated perfused rat heart. J. Appl. Physiol 40, 1004–1008, doi:10.1152/jappl.1976.40.6.1004 (1976). [PubMed: 931918]
51. Valvona CJ, Fillmore HL, Nunn PB & Pilkington GJ The Regulation and Function of Lactate Dehydrogenase A: Therapeutic Potential in Brain Tumor. Brain Pathol. 26, 3–17, doi:10.1111/bpa.12299 (2016). [PubMed: 26269128]
52. Bonen A Lactate transporters (MCT proteins) in heart and skeletal muscles. Med. Sci. Sports Exerc. 32, 778–789 (2000). [PubMed: 10776897]

53. Draoui N & Feron O Lactate shuttles at a glance: from physiological paradigms to anti-cancer treatments. Dis. Model. Mech 4, 727–732, doi:10.1242/dmm.007724 (2011). [PubMed: 22065843]
54. Chen W & Frangogiannis NG Fibroblasts in post-infarction inflammation and cardiac repair. Biochim. Biophys. Acta 1833, 945–953, doi:10.1016/j.bbamcr.2012.08.023 (2013). [PubMed: 22982064]
55. van den Borne SW et al. Molecular imaging of interstitial alterations in remodeling myocardium after myocardial infarction. J. Am. Coll. Cardiol 52, 2017–2028, doi:10.1016/j.jacc.2008.07.067 (2008). [PubMed: 19055994]
56. Mewton N, Liu CY, Croisille P, Bluemke D & Lima JA Assessment of myocardial fibrosis with cardiovascular magnetic resonance. J. Am. Coll. Cardiol 57, 891–903, doi:10.1016/j.jacc.2010.11.013 (2011). [PubMed: 21329834]
57. Messroghli DR et al. Myocardial T1 mapping: application to patients with acute and chronic myocardial infarction. Magn. Reson. Med 58, 34–40, doi:10.1002/mrm.21272 (2007). [PubMed: 17659622]
58. Ho CY et al. Myocardial fibrosis as an early manifestation of hypertrophic cardiomyopathy. N. Engl. J. Med 363, 552–563, doi:10.1056/NEJMoa1002659 (2010). [PubMed: 20818890]
59. Weber KT et al. Collagen remodeling of the pressure-overloaded, hypertrophied nonhuman primate myocardium. Circ. Res 62, 757–765 (1988). [PubMed: 2964945]
60. Yong KW et al. Mechanoregulation of cardiac myofibroblast differentiation: implications for cardiac fibrosis and therapy. Am. J. Physiol. Heart Circ. Physiol. 309, H532–542, doi:10.1152/ajpheart.00299.2015 (2015). [PubMed: 26092987]
61. Trickey WR, Lee GM & Guilak F Viscoelastic properties of chondrocytes from normal and osteoarthritic human cartilage. J. Orthop. Res 18, 891–898, doi:10.1002/jor.1100180607 (2000). [PubMed: 11192248]
62. Richardson WJ, Clarke SA, Quinn TA & Holmes JW Physiological Implications of Myocardial Scar Structure. Compr Physiol 5, 1877–1909, doi:10.1002/cphy.c140067 (2015). [PubMed: 26426470]
63. Herum KM, Choppe J, Kumar A, Engler AJ & McCulloch AD Mechanical regulation of cardiac fibroblast profibrotic phenotypes. Mol. Biol. Cell 28, 1871–1882, doi:10.1091/mbc.E17-01-0014 (2017). [PubMed: 28468977]
64. Lou Q, Janardhan A & Efimov IR Remodeling of calcium handling in human heart failure. Adv. Exp. Med. Biol 740, 1145–1174, doi:10.1007/978-94-007-2888-2_52 (2012). [PubMed: 22453987]
65. Bhar-Amato J, Davies W & Agarwal S Ventricular Arrhythmia after Acute Myocardial Infarction: ‘The Perfect Storm’. Arrhythm Electrophysiol Rev 6, 134–139, doi:10.15420/aer.2017.24.1 (2017). [PubMed: 29018522]
66. Huisken J & Stainier DY Selective plane illumination microscopy techniques in developmental biology. Development 136, 1963–1975, doi:10.1242/dev.022426 (2009). [PubMed: 19465594]
67. Truong TV, Supatto W, Koos DS, Choi JM & Fraser SE Deep and fast live imaging with two-photon scanned light-sheet microscopy. Nat. Methods 8, 757–760, doi:10.1038/nmeth.1652 (2011). [PubMed: 21765409]
68. Morita N, Mandel WJ, Kobayashi Y & Karagueuzian HS Cardiac fibrosis as a determinant of ventricular tachyarrhythmias. J Arrhythm 30, 389–394, doi:10.1016/j.joa.2013.12.008 (2014). [PubMed: 25642299]
69. Duan Q et al. BET bromodomain inhibition suppresses innate inflammatory and profibrotic transcriptional networks in heart failure. Sci. Transl. Med 9, doi:10.1126/scitranslmed.aah5084 (2017).
70. Mehta LS et al. Cardiovascular Disease and Breast Cancer: Where These Entities Intersect: A Scientific Statement From the American Heart Association. Circulation 137, e30–e66, doi:10.1161/CIR.0000000000000556 (2018). [PubMed: 29437116]
71. Patnaik JL, Byers T, DiGuiseppi C, Dabelea D & Denberg TD Cardiovascular disease competes with breast cancer as the leading cause of death for older females diagnosed with breast cancer: a retrospective cohort study. Breast Cancer Res. 13, R64, doi:10.1186/bcr2901 (2011). [PubMed: 21689398]

72. Salz T et al. Preexisting Cardiovascular Risk and Subsequent Heart Failure Among Non-Hodgkin Lymphoma Survivors. J. Clin. Oncol 35, 3837–3843, doi:10.1200/JCO.2017.72.4211 (2017). [PubMed: 28922087]
73. Narayan HK et al. Detailed Echocardiographic Phenotyping in Breast Cancer Patients: Associations With Ejection Fraction Decline, Recovery, and Heart Failure Symptoms Over 3 Years of Follow-Up. Circulation 135, 1397–1412, doi:10.1161/CIRCULATIONAHA.116.023463 (2017). [PubMed: 28104715]
74. Arafa MH, Mohammad NS, Atteia HH & Abd-Elaziz HR Protective effect of resveratrol against doxorubicin-induced cardiac toxicity and fibrosis in male experimental rats. J. Physiol. Biochem 70, 701–711, doi:10.1007/s13105-014-0339-y (2014). [PubMed: 24939721]
75. Torti FM et al. Cardiotoxicity of epirubicin and doxorubicin: assessment by endomyocardial biopsy. Cancer Res. 46, 3722–3727 (1986). [PubMed: 3458531]
76. Mortensen SA, Olsen HS & Baandrup U Chronic anthracycline cardiotoxicity: haemodynamic and histopathological manifestations suggesting a restrictive endomyocardial disease. Br. Heart J. 55, 274–282 (1986). [PubMed: 3456785]
77. Tham EB et al. Diffuse myocardial fibrosis by T1-mapping in children with subclinical anthracycline cardiotoxicity: relationship to exercise capacity, cumulative dose and remodeling. J. Cardiovasc. Magn. Reson 15, 48, doi:10.1186/1532-429X-15-48 (2013). [PubMed: 23758789]
78. Zamorano JL et al. 2016 ESC Position Paper on cancer treatments and cardiovascular toxicity developed under the auspices of the ESC Committee for Practice Guidelines: The Task Force for cancer treatments and cardiovascular toxicity of the European Society of Cardiology (ESC). Eur. Heart J. 37, 2768–2801, doi:10.1093/eurheartj/ehw211 (2016). [PubMed: 27567406]
79. Stevens KR & Murry CE Human Pluripotent Stem Cell-Derived Engineered Tissues: Clinical Considerations. Cell Stem Cell 22, 294–297, doi:10.1016/j.stem.2018.01.015 (2018). [PubMed: 29499147]
80. Forte E, Furtado MB & Rosenthal N The interstitium in cardiac repair: role of the immune-stromal cell interplay. Nat. Rev. Cardiol 15, 601–616, doi:10.1038/s41569-018-0077-x (2018). [PubMed: 30181596]
81. Leopold JA & Loscalzo J Emerging Role of Precision Medicine in Cardiovascular Disease. Circ. Res 122, 1302–1315, doi:10.1161/CIRCRESAHA.117.310782 (2018). [PubMed: 29700074]
82. Santolini M et al. A personalized, multiomics approach identifies genes involved in cardiac hypertrophy and heart failure. NPJ Syst Biol Appl 4, 12, doi:10.1038/s41540-018-0046-3 (2018). [PubMed: 29507758]
83. van den Heuvel NH, van Veen TA, Lim B & Jonsson MK Lessons from the heart: mirroring electrophysiological characteristics during cardiac development to in vitro differentiation of stem cell derived cardiomyocytes. J. Mol. Cell. Cardiol 67, 12–25, doi:10.1016/j.yjmcc.2013.12.011 (2014). [PubMed: 24370890]
84. Davis-Turak J et al. Genomics pipelines and data integration: challenges and opportunities in the research setting. Expert Rev. Mol. Diagn 17, 225–237, doi:10.1080/14737159.2017.1282822 (2017). [PubMed: 28092471]
85. Martin M Cutadapt removes adapter sequences from high-throughput sequencing reads. 2011 17, pp. 10–12, doi:10.14806/ej.17.1.200 (2011).
86. Kim D et al. TopHat2: accurate alignment of transcriptomes in the presence of insertions, deletions and gene fusions. Genome Biol. 14, R36, doi:10.1186/gb-2013-14-4-r36 (2013). [PubMed: 23618408]
87. Langmead B & Salzberg SL Fast gapped-read alignment with Bowtie 2. Nat. Methods 9, 357–359, doi:10.1038/nmeth.1923 (2012). [PubMed: 22388286]
88. Anders S, Pyl PT & Huber W HTSeq--a Python framework to work with high-throughput sequencing data. Bioinformatics 31, 166–169, doi:10.1093/bioinformatics/btu638 (2015). [PubMed: 25260700]
89. Love MI, Huber W & Anders S Moderated estimation of fold change and dispersion for RNA-seq data with DESeq2. Genome Biol. 15, 550, doi:10.1186/s13059-014-0550-8 (2014). [PubMed: 25516281]

90. Draghici S et al. A systems biology approach for pathway level analysis. Genome Res. 17, 1537–1545, doi:10.1101/gr.6202607 (2007). [PubMed: 17785539]
91. Hannenhalli S et al. Transcriptional genomics associates FOX transcription factors with human heart failure. Circulation 114, 1269–1276, doi:10.1161/CIRCULATIONAHA.106.632430 (2006). [PubMed: 16952980]
92. Smyth GK Linear models and empirical bayes methods for assessing differential expression in microarray experiments. Stat. Appl. Genet. Mol. Biol 3, Article3, doi:10.2202/1544-6115.1027 (2004).
93. Ritchie ME et al. limma powers differential expression analyses for RNA-sequencing and microarray studies. Nucleic Acids Res. 43, e47, doi:10.1093/nar/gkv007 (2015). [PubMed: 25605792]
94. Davis S & Meltzer PS GEOquery: a bridge between the Gene Expression Omnibus (GEO) and BioConductor. Bioinformatics 23, 1846–1847, doi:10.1093/bioinformatics/btm254 (2007). [PubMed: 17496320]
95. Jol SJ Make a Venn Diagram, <https://www.stefanjol.nl/venny> (2015).
96. Ignatchenko V, Ignatchenko A, Sinha A, Boutros PC & Kislinger T VennDIS: a JavaFX-based Venn and Euler diagram software to generate publication quality figures. Proteomics 15, 1239–1244, doi:10.1002/pmic.201400320 (2015). [PubMed: 25545689]
97. Chen J, Bardes EE, Aronow BJ & Jegga AG ToppGene Suite for gene list enrichment analysis and candidate gene prioritization. Nucleic Acids Res. 37, W305–311, doi:10.1093/nar/gkp427 (2009). [PubMed: 19465376]
98. Yang KC et al. Deep RNA sequencing reveals dynamic regulation of myocardial noncoding RNAs in failing human heart and remodeling with mechanical circulatory support. Circulation 129, 1009–1021, doi:10.1161/CIRCULATIONAHA.113.003863 (2014). [PubMed: 24429688]
99. Ounzain S et al. Genome-wide profiling of the cardiac transcriptome after myocardial infarction identifies novel heart-specific long non-coding RNAs. Eur. Heart J. 36, 353–368a, doi:10.1093/eurheartj/ehu180 (2015). [PubMed: 24786300]
100. Subramanian A et al. Gene set enrichment analysis: a knowledge-based approach for interpreting genome-wide expression profiles. Proc. Natl. Acad. Sci. U. S. A 102, 15545–15550, doi:10.1073/pnas.0506580102 (2005). [PubMed: 16199517]
101. Huang S, Heikal AA & Webb WW Two-photon fluorescence spectroscopy and microscopy of NAD(P)H and flavoprotein. Biophys. J 82, 2811–2825, doi:10.1016/S0006-3495(02)75621-X (2002). [PubMed: 11964266]
102. Russell S, Wojtkowiak J, Neilson A & Gillies RJ Metabolic Profiling of healthy and cancerous tissues in 2D and 3D. Sci. Rep 7, 15285, doi:10.1038/s41598-017-15325-5 (2017). [PubMed: 29127321]
103. Sato M, Theret DP, Wheeler LT, Ohshima N & Nerem RM Application of the micropipette technique to the measurement of cultured porcine aortic endothelial cell viscoelastic properties. J. Biomech. Eng 112, 263–268 (1990). [PubMed: 2214707]
104. Theret DP, Levesque MJ, Sato M, Nerem RM & Wheeler LT The application of a homogeneous half-space model in the analysis of endothelial cell micropipette measurements. J. Biomech. Eng 110, 190–199 (1988). [PubMed: 3172738]
105. Edelstein AD et al. Advanced methods of microscope control using muManager software. J Biol Methods 1, doi:10.14440/jbm.2014.36 (2014).

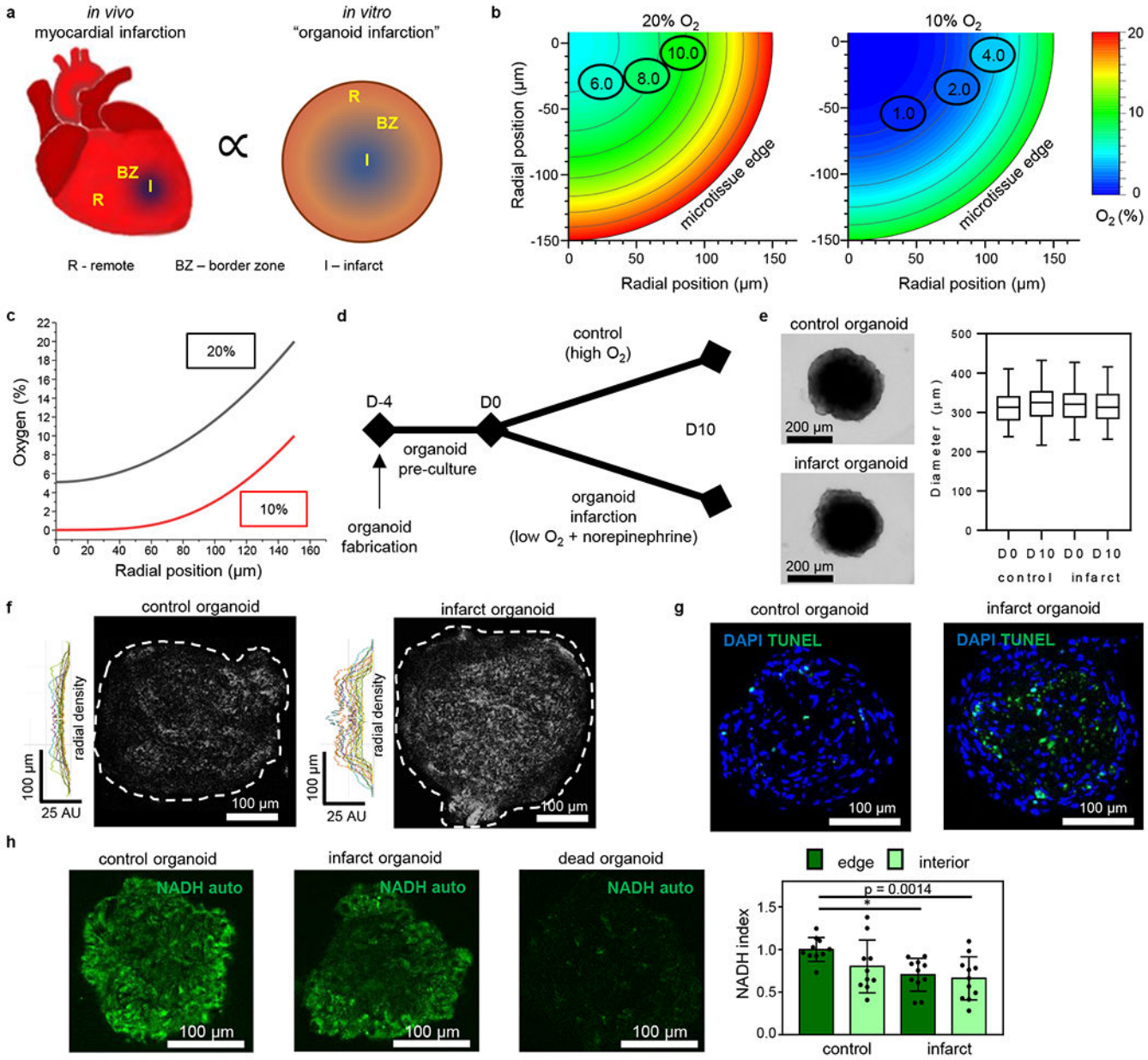

Fig. 1 |. Development of human 3D post-myocardial infarction organoid model.

a, The 3D nature and diffusion limitations in post-myocardial infarction (MI) hearts can be spatially mimicked to create an in vitro post-MI model (infarct organoid). **b, c**, Finite element modeling and quantification of oxygen diffusion in simulated cardiac microtissues provide a guiding design principle for an in vitro infarction protocol, revealing the inherent oxygen diffusion limitation at 20% and 10% external oxygen. **d**, Control and cardiac organoid infarction protocol timeline using altered oxygen (O_2) and norepinephrine (NE) in culture for 10 days (D10). **e**, Bright-field images of organoids on D10 and diameters (mean ± standard deviation) on D0 and D10. n= 252, 215 (D0, D10) organoids in control group; 152, 216 (D0, D10) infarct organoids in test group; 9, 5, 9, 7 wells per D0 control, D0 infarct, D10 control, D10 infarct groups, respectively; 1 donor (Donor A). For box-plots,

center line - median; box limits - upper and lower quartiles; whiskers - total range. **f**, Confocal z-slice images (>30 μm below organoid surface) of hypoxia-activated Image-iT Green Hypoxia live-cell stain on D10 with radial density profile plots of normalized integrated intensities, indicating lower oxygen (brighter) toward interior of infarct organoids compared to control organoids. n= 13 organoids in control group; 15 infarct organoids in test group; 3 wells per group; 1 donor (Donor A). **g**, Z-stack confocal images (from 18 control and 11 infarct organoid images) of TUNEL apoptosis staining of D10 control and infarct organoid frozen sections showing apoptotic core in infarct organoids. **h**, NADH autofluorescence from live two-photon imaging (z-slice >30 μm below surface) of live control, infarct, and dead (frozen+thaw) cardiac organoids on D10 (left) and NADH index quantification (right) (mean ± standard deviation) showing lower NADH in center of organoids and overall lower levels in infarct organoids. *$p<0.001$ using one-way ANOVA with Bonferroni-corrected two-sided t-test post-hoc. n= 10 organoids in control group; 11 infarct organoids in test group; 3 wells per group; 1 donor (Donor A).

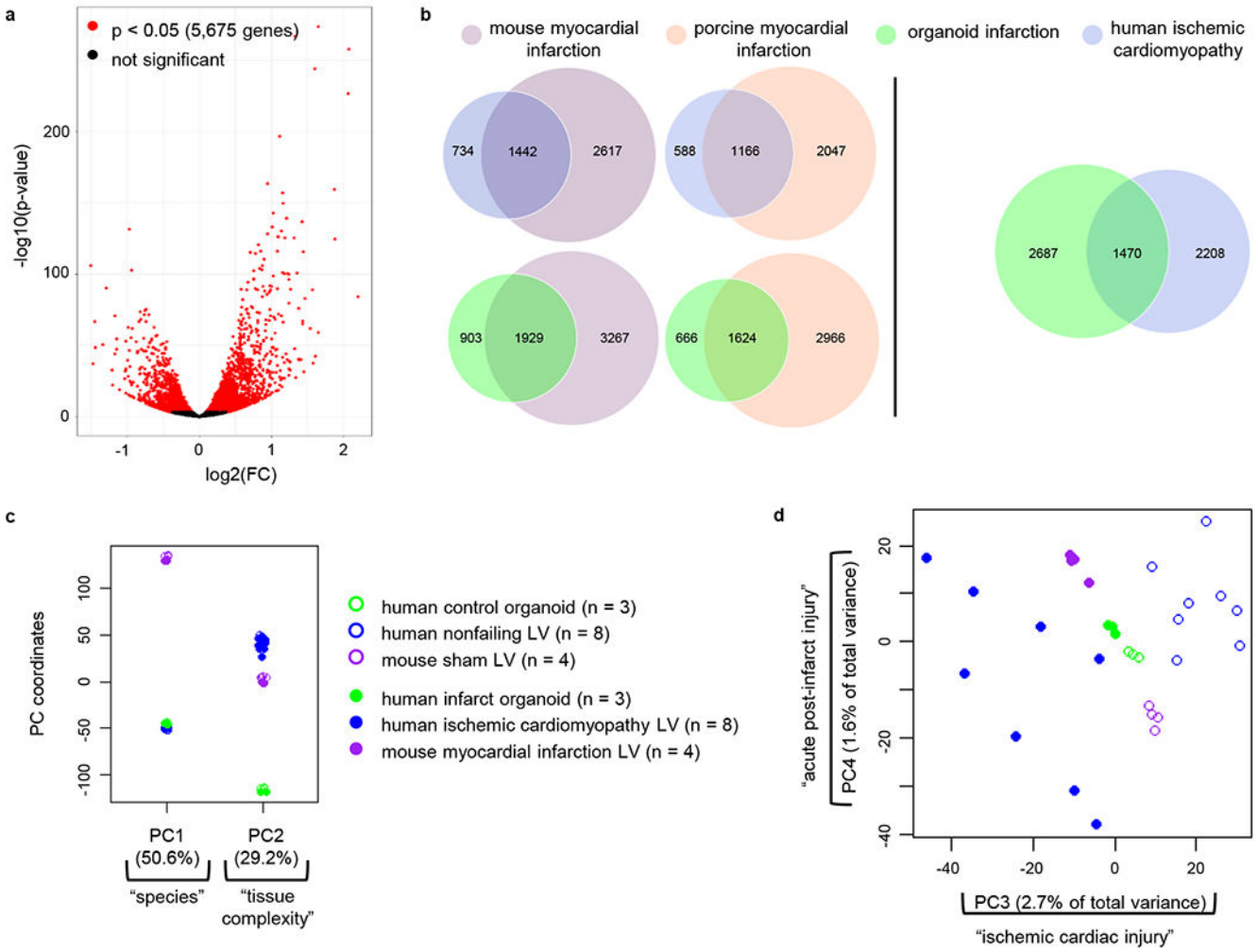

Fig. 2 |. Human in vitro 3D post-myocardial infarction (MI) organoids share global gene expression profile with adult human ischemic cardiomyopathy and animal acute post-MI samples.

a, Distribution of gene expression and fold change (FC) (black) with differentially expressed (DE) genes (red) of infarct organoids compared to control organoids after day 10. DE analysis can be found in Methods. **b**, Comparison of DE ($p<0.05$) genes from infarct organoids (vs. control organoids) RNA sequencing data compared to human ischemic cardiomyopathy (vs. nonfailing), mouse 1 week post-MI (vs. sham), and pig 1 week post-MI (vs. sham) microarray data. Sample sizes and DE analysis for transcriptomic data can be found in Methods. **c, d**, Principal component analysis of the 4,765 shared genes between the cardiac organoid samples and mouse 2 week post-MI and human ischemic cardiomyopathy RNA sequencing samples showing the systems-level relevance of cardiac infarct organoids in modeling injured myocardium. n = 3 biologically independent samples for human control and infarct organoids, n = 8 biologically independent human ischemic cardiomyopathy left ventricles and nonfailing left ventricle samples, n = 4 biological independent mouse myocardial infarction left ventricle and sham left ventricle samples.

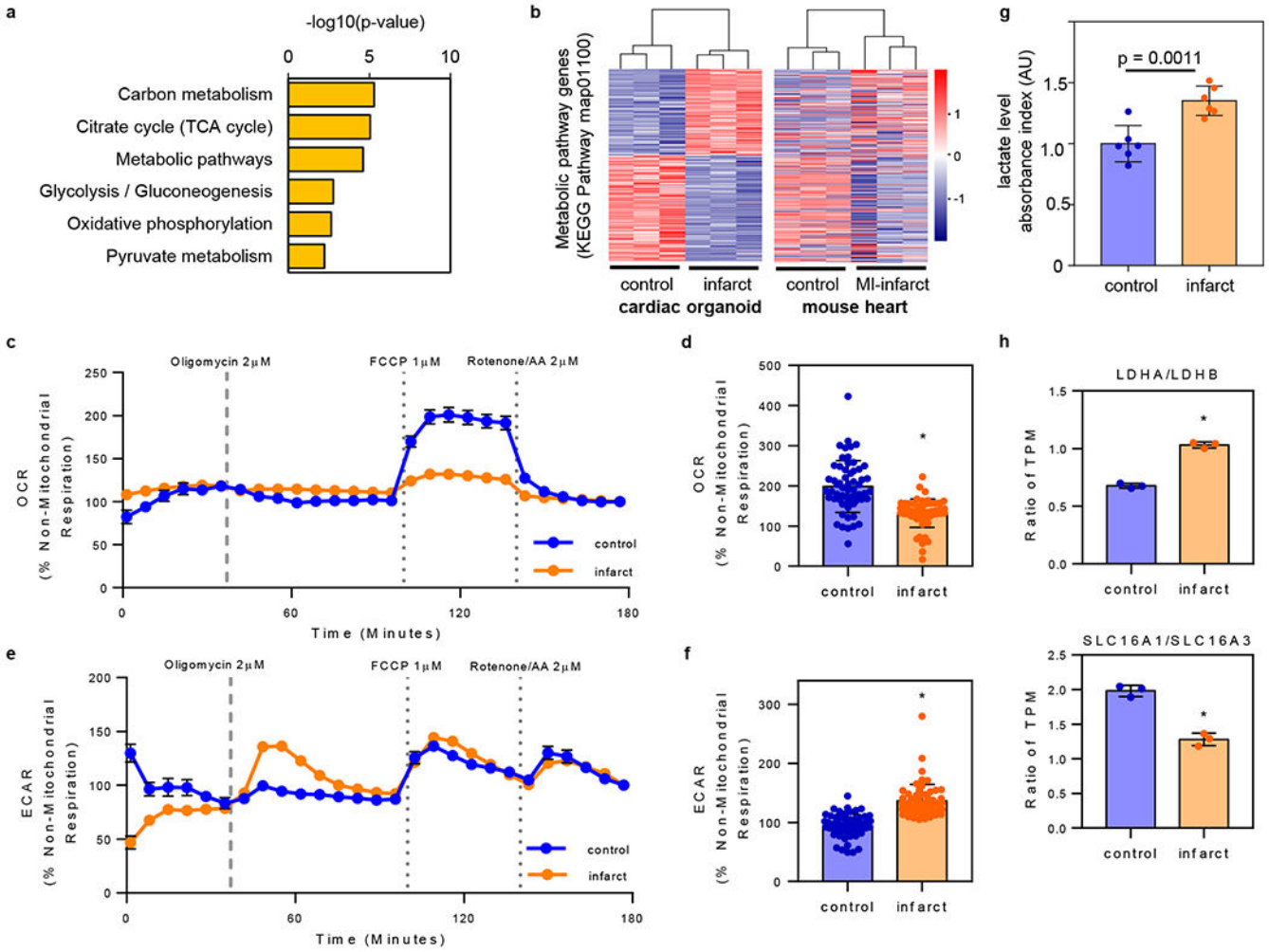

Fig. 3 |. Cardiac infarct organoids model pathological metabolic responses at the transcriptomic, functional, and tissue level.

a, Significant ($p<0.05$) gene ontology terms based on differentially expressed (DE) genes between control and infarct organoids on D10 compiled using Advaita Bio's iPathwayGuide. Organoid samples, n= 3 biologically independent samples per group (each sample containing 1 well of 30-35 organoids), 1 donor (Donor A). DE analysis can be found in Methods. **b**, Heatmap of DE genes in the "metabolic pathway" (KEGG Pathway map01100) in organoid model showing similar trends in gene expression changes after injury compared to mouse 1 week post-myocardial infarction (MI) microarray data. Scale is row z-score. Organoid samples, n= 3 biologically independent samples per group (each sample containing 1 well of 30-35 organoids), 1 donor (Donor A); mouse, n= 3 biologically independent samples per group. **c, e**, Oxygen consumption rate (OCR) and extracellular acidification rate (ECAR) during Seahorse mitochondrial stress test of D10 control and infarct organoids with **d, f**, peak OCR after carbonyl cyanide-p-trifluoromethoxyphenylhydrazone (FCCP) addition and peak ECAR after Oligomycine addition. n= 59 organoids in the control group; 59 infarct organoids in the test group; 3 wells per group; 1 donor (Donor A). Mean ± standard deviation. *$p<0.001$ using Student's two-

sided t-test. **g**, Normalized L-lactate levels (based on absorbance readings) relative to control media measured in D10 organoid media. n= 6 wells per group, 1 donor (Donor A). P-value from Student's two-sided t-test. **h**, Differences of lactate-related gene expression (ratio of transcripts per million – TPM) from RNA sequencing data between control and infarct organoids on D10. Mean ± standard deviation. *$p<0.001$ using Student's two-sided t-test.

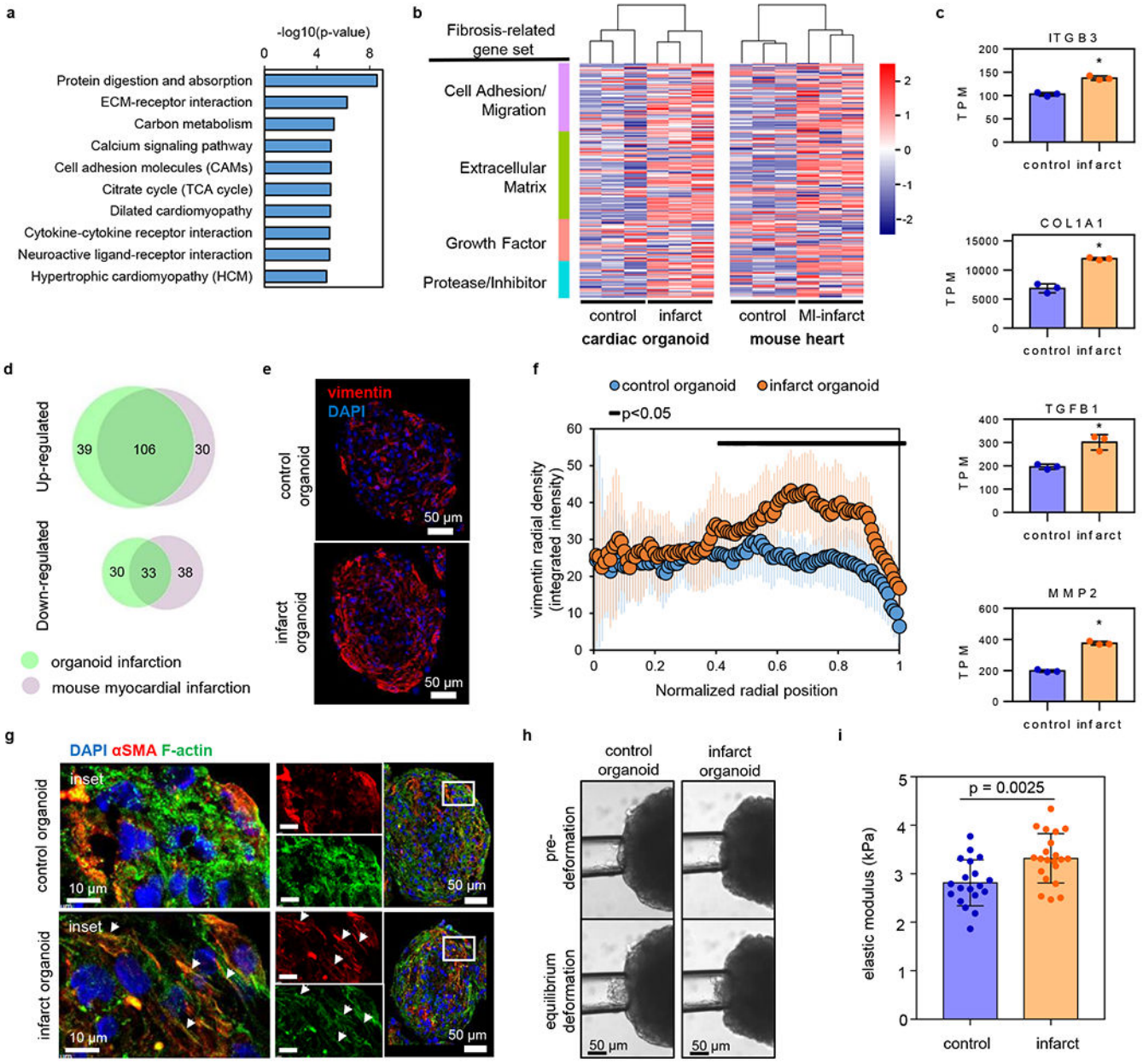

Fig. 4 |. Cardiac infarct organoids model pathological fibrosis response at the transcriptomic, cellular, and tissue level.

a, Top identified pathways from organoid RNA sequencing data. Organoid samples, n= 3 biologically independent samples per group (each sample containing 1 well of 30-35 organoids), 1 donor (Donor A). DE analysis can be found in Methods. **b**, Heatmap of fibrosis-related gene set in organoid model compared to mouse 1 week post-myocardial infarction (MI) microarray data. Scale is row z-score. Organoid samples, n= 3 biologically independent samples per group (each sample containing 1 well of 30-35 organoids), 1 donor (Donor A); mouse, n= 3 biologically independent samples per group. **c**, Representative fibrosis-related genes (transcripts per million – TPM) from organoid RNA sequencing indicate significant changes in infarct organoids (mean ± standard deviation). *p<0.001

using DESeq2 differential expression analysis of sequencing data. Organoid samples, n= 3 biologically independent samples per group (each sample containing 1 well of 30-35 organoids), 1 donor (Donor A). **d**, Venn diagram of fibrosis-related genes show similar trends in gene expression changes after injury in infarct organoid and mouse 1 week post-MI microarray data. n= 3 biologically independent samples per group. **e, f**, Confocal z-stack images of vimentin immunofluorescent staining of control and infarct organoid sections with vimentin radial density profile plots of normalized integrated intensities. n= 15 organoids in the control group; 15 infarct organoids in the test group; 3 wells per group; 1 donor (Donor A). Mean ± standard deviation. Student's two-sided t-test was used for statistical significance (p-values can be found in Table S5). **g**, Confocal z-stack images (from 10 images per group) of immunofluorescently stained myofibroblast-like cells in organoid sections indicated by fibrillar structures (white arrows) with alpha smooth muscle actin (αSMA)/F-actin (phalloidin) colocalization that are not seen in control organoids. **h**, Bright-field images (from 19 control and 21 infarct organoid images) of micropipette aspiration tests. **i**, Stiffness (i.e., elastic modulus, kPa) calculated using equilibrium deformation displacement (mean ± standard deviation). n= 19 organoids in the control group; 21 infarct organoids in the test group; 3 wells per group; 1 donor (Donor A). P-value from Student's two-sided t-test.

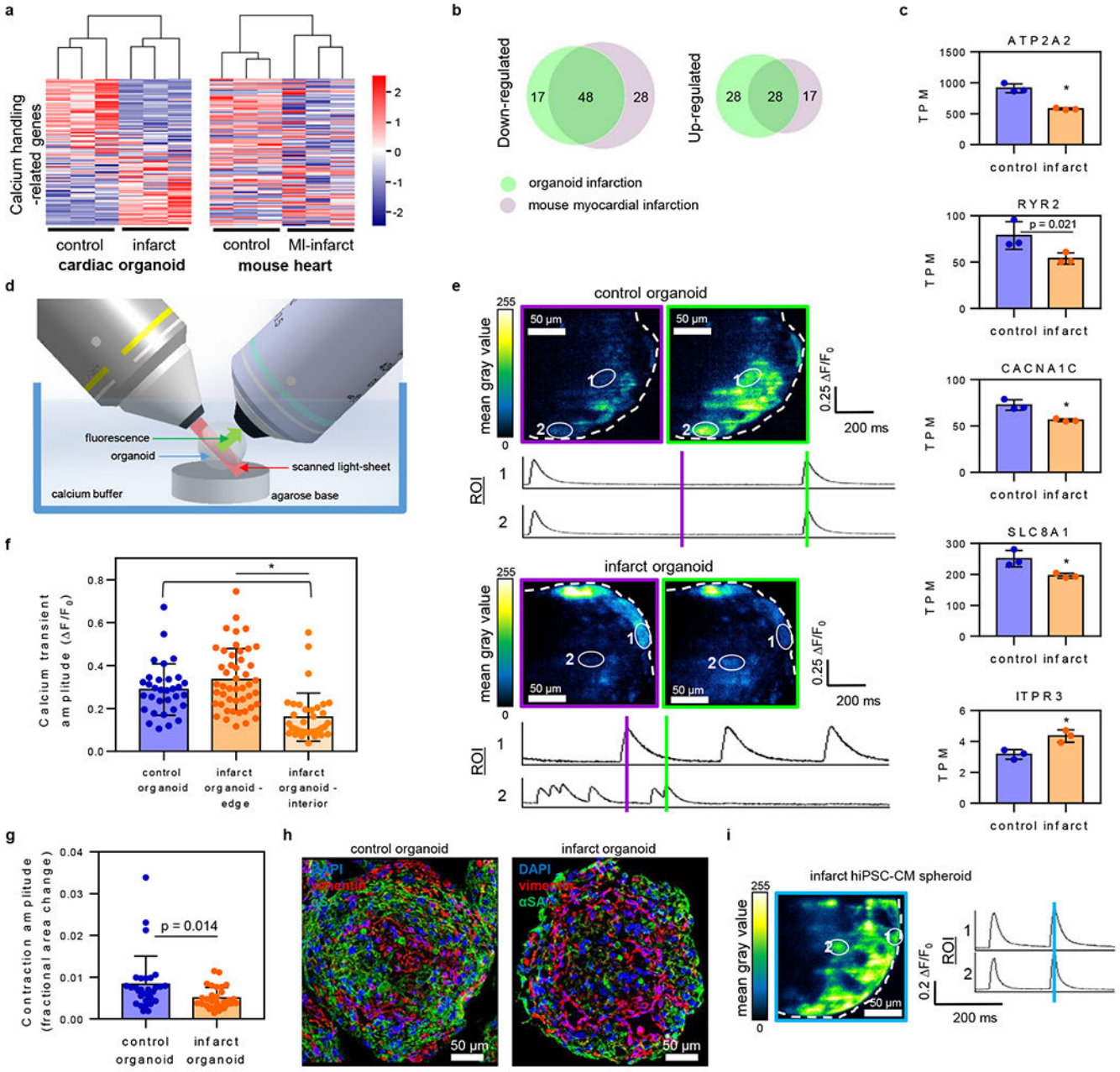

Fig. 5 |. Tissue-level pathological calcium-handling in cardiac infarct organoids observed with in situ imaging of the interior of live cardiac organoids.

a, b, Calcium handling-related gene set in organoid model showing similar trends in gene expression changes after injury compared to mouse 1 week post-myocardial infarction (MI) microarray data. Scale is row z-score. Organoid samples, n= 3 biologically independent samples per group (each sample containing 1 well of 30-35 organoids), 1 donor (Donor A); mouse, n= 3 biologically independent samples per group. **c**, Representative calcium-handling genes (transcripts per million – TPM) from organoid RNA sequencing indicating significant change to major calcium handling genes (mean ± standard deviation). *p<0.001 using DESeq2 differential expression analysis of sequencing data. Organoid samples, n= 3

biologically independent samples per group (each sample containing 1 well of 30-35 organoids), 1 donor (Donor A). **d**, Illustration of customized Two-Photon scanned Light-Sheet Microscope (2PLSM) for in situ imaging of live cardiac organoids. **e**, 2PLSM imaging (from 10 control and 19 infarct organoid images) from selected imaging planes at >50 μm below organoid surface of D10 control and infarct organoids containing GCaMP6-labeled human induced pluripotent stem cell-derived-cardiomyocytes (hiPSC-CMs) with calcium transient profiles corresponding to the two edge and interior cardiomyocyte regions of interest (ROIs) showing unsynchronization in infarct organoids. **f**, Quantification of calcium transient amplitude ($\Delta F/F_0$) of separate ROIs representing individual cardiomyocytes from selected imaging planes at >50 μm below organoid surface. n= 32 ROIs across 10 control organoids, 47 edge ROIs and 35 interior ROIs across 19 infarct organoids; 3 wells per group; 1 donor (Donor A). Mean ± standard deviation. *$p<0.001$ using one-way ANOVA with Bonferroni-corrected two-sided t-test post-hoc. **g,** Contraction amplitude (fractional area change) of organoids on D10 showing significant decrease in contractile function in infarct organoids. n= 30 organoids in the control group; 30 infarct organoids in the test group; 5 wells per group; 1 donor (Donor A). Mean ± standard deviation. P-value from Student's two-sided t-test. **h**, Confocal z-stack images (from 26 control and 27 infarct organoid images) of immunofluorescent staining of organoid sections on D10 showing interconnected alpha sarcomeric actinin (αSA)-positive (green) cardiomyocytes in control organoids and separation of edge and interior cardiomyocytes by vimentin-positive (red) cells in infarct organoids. **i**, 2PLSM imaging (from 3 control and 4 infarct organoid images) from selected imaging planes at >50 μm below surface of GCaMP6-labeled hiPSC-CM spheroids with calcium transient profiles corresponding to the two edge and interior cardiomyocyte ROIs showing synchronization in infarct hiPSC-CM spheroids.

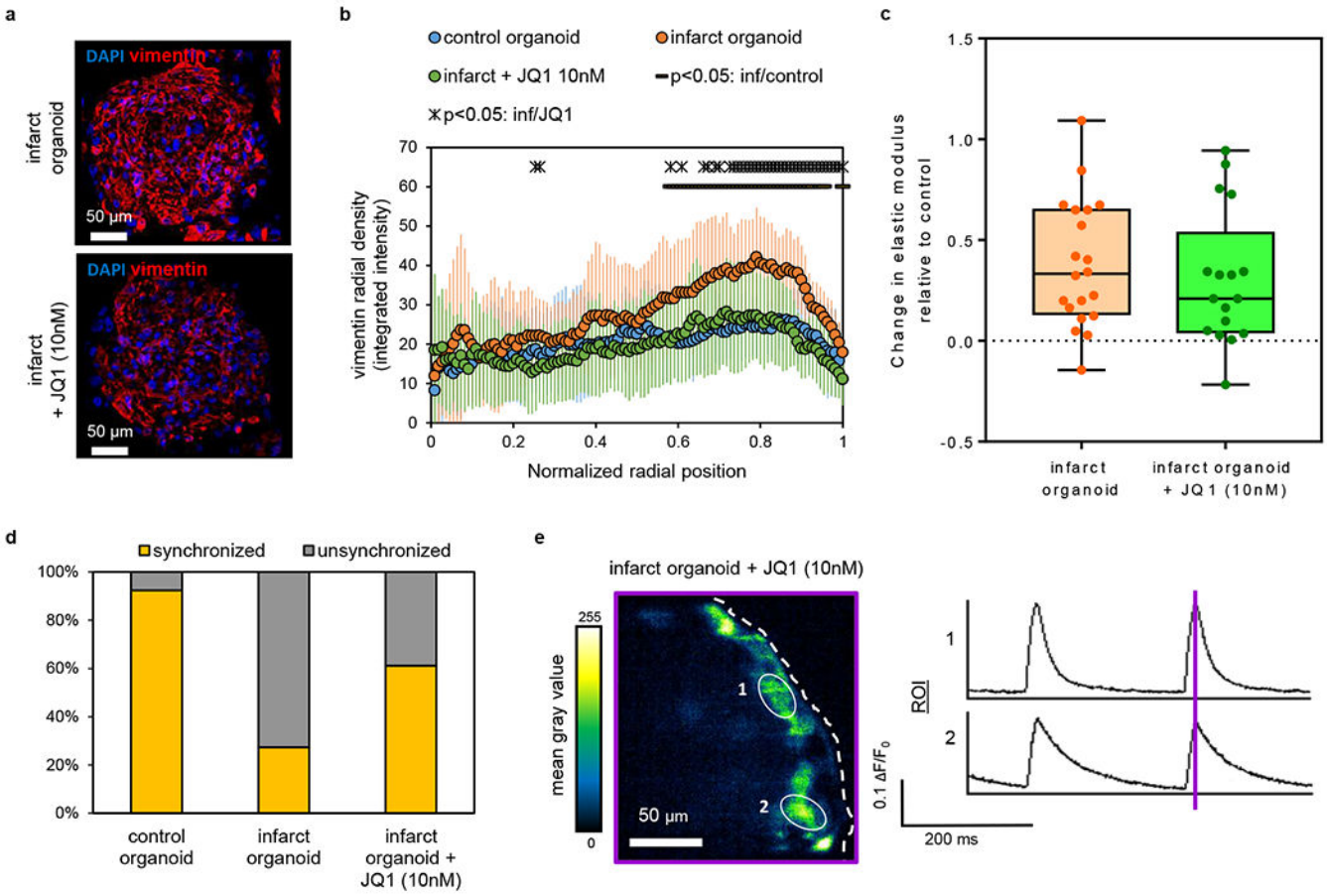

Fig. 6 |. Human cardiac infarct organoids for tissue-level heart failure drug testing.

a, b, Confocal z-stack images of vimentin immunofluorescent staining of D10 infarct organoid sections with or without “anti-fibrotic” (JQ1, 10 nM) culture conditions and associated vimentin radial density profile plots of normalized integrated intensities. n= 14 organoids in control group; 13 infarct organoids in infarct test group; 12 infarct organoids in JQ1 test group; 3 wells per group; 1 donor (Donor A). Mean ± standard deviation. Student’s two-sided t-test was used for statistical significance (p-values can be found in Table S5). **c**, Change in elastic modulus relative to control on D10 for cardiac infarction protocol with added “anti-fibrotic” (JQ1, 10 nM) culture conditions. n= 20 infarct organoids in the infarct test group; 17 infarct organoids in the JQ1 test group; 3 wells per group; 1 donor (Donor A). For box-plots, center line - median; box limits - upper and lower quartiles; whiskers - total range. Differences between groups were not significant using Student’s t-test. **d**, Proportion of organoids (control, infarct, infarct with “anti-fibrotic” treatment (JQ1, 10 nM)) that exhibited synchronized or unsynchronized beating. n= 66 organoids in the control group; 66 infarct organoids in the infarct test group; 72 infarct organoids in the JQ1 test group; 3 wells per group; 1 donor (Donor A). **e,** 2PLSM imaging (from 6 organoid images) of infarct organoids treated with JQ1 (10 nM) during infarction protocol from selected imaging planes at >50 μm below organoid surface showing synchronization of cardiomyocyte regions of interest.

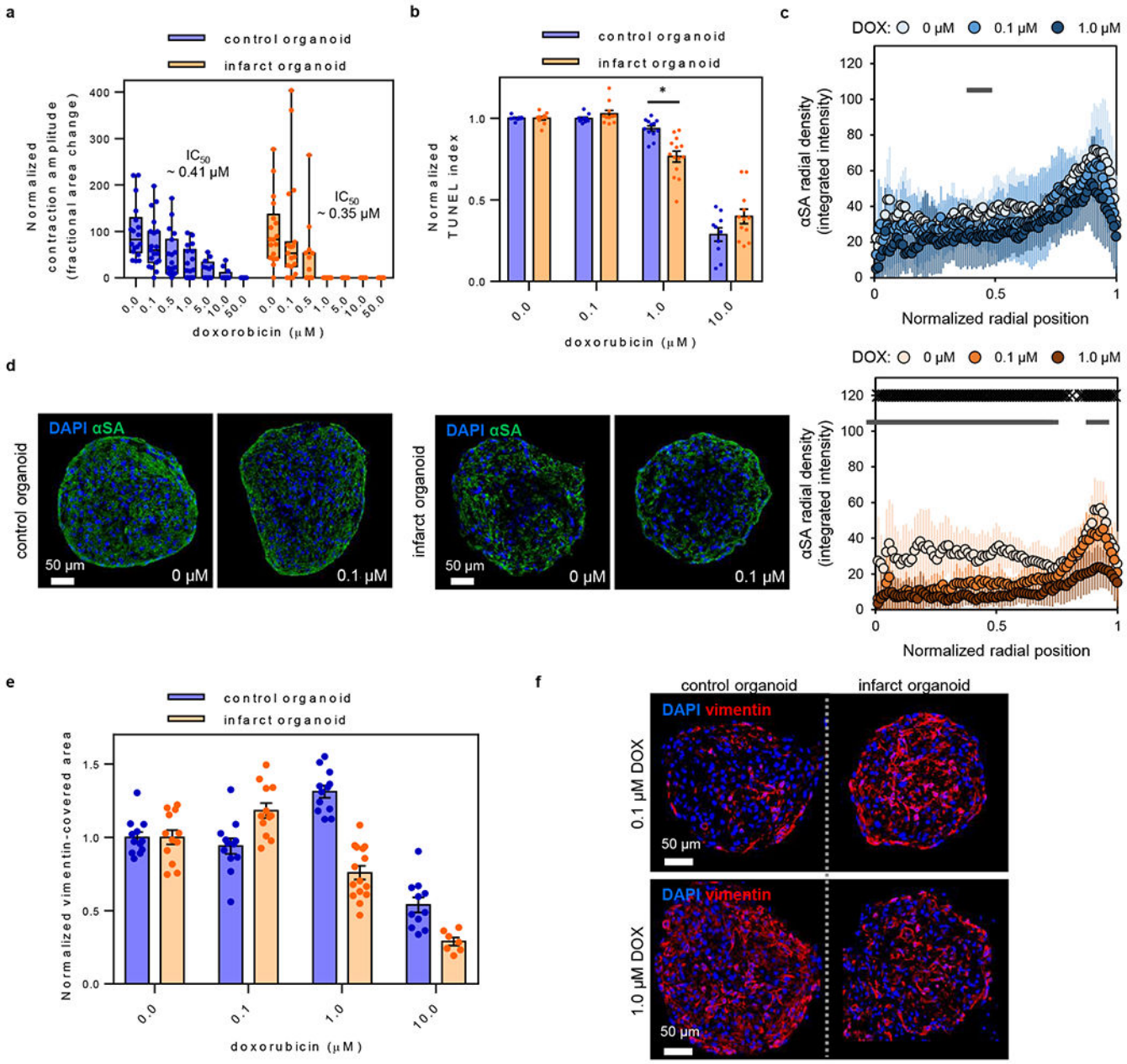

Fig. 7 |. Detection of tissue-level drug-induced exacerbation of cardiotoxicity using cardiac infarct organoids.

a, Normalized contraction amplitude (relative to vehicle control of each group) with IC_{50} of organoids in response to doxorubicin (DOX). n= 18, 19, 19, 18, 12, 12, 11 (at 0, 0.1, 0.5, 1.0, 5.0, 10.0, 50.0 μM doses of DOX) organoids in control group; 18, 19, 18, 17, 11, 11, 11 (at 0, 0.1, 0.5, 1.0, 5.0, 10.0, 50.0 μM doses of DOX) infarct organoids in test group; 3 wells per group; 1 donor (Donor A). For box-plots, center line - median; box limits - upper and lower quartiles; whiskers - total range. **b**, Normalized viability index (relative to vehicle control of each group) based on TUNEL-apoptotic staining of organoid sections after DOX exposure. n= 10, 10, 12, 10 (at 0, 0.1, 1.0, 10.0 μM doses of DOX) organoids in control

group; 11, 11, 14, 12 (at 0, 0.1, 1.0, 10.0 μM doses of DOX) infarct organoids in test group; 3 wells per group; 1 donor (Donor A). *$p<0.001$ using two-way ANOVA with Tukey post-hoc. Mean ± standard deviation. **c**, Sarcomeric changes caused by increased dose of DOX quantified by radial density profile plots of normalized integrated intensities of alpha sarcomeric (αSA) immunofluorescent staining in organoid sections. n= 9, 8, 10 (at 0, 0.1, 1.0 μM doses of DOX) organoids in control group; 11, 10, 14 (at 0, 0.1, 1.0 μM doses of DOX) infarct organoids in test group; 3 wells per group; 1 donor (Donor A). -- represents $p<0.05$ for 0.1 μM versus 0 μM DOX; x represents $p<0.05$ for 1.0 μM versus 0 μM DOX using Student's two-sided t-test (p-values can be found in Table S5). Mean ± standard deviation. **d**, Confocal z-stack images (from 17 control and 21 infarct organoid images) of αSA (green) visualizing the larger relative change in interior contractile structures from 0 μM to 0.1 μM DOX in infarct organoids than in control organoids. **e**, DOX-induced changes in vimentin-covered area (relative to vehicle control of each group) in organoid sections. n= 12, 12, 12, 11 (at 0, 0.1, 1.0, 10.0 μM doses of DOX) organoids in the control group; 12, 12, 15, 7 (at 0, 0.1, 1.0, 10.0 μM doses of DOX) infarct organoids in the test group; 3 wells per group; 1 donor (Donor A). Two-way ANOVA with Tukey post-hoc was used for statistical significance (p-values can be found in Table S7). Mean ± standard deviation. **f,** Confocal z-stack images (from 24 control and 27 infarct organoid images) of relative differences in vimentin-covered area in control and infarct organoids at 0.1 and 1 μM DOX. All DOX exposure was 48 hrs starting on D10.

Table 1 |

Gene set enrichment of Gene ontology of principal component (PC) 3 and 4 using PC gene loadings.

Principal Component 3 – "ischemic cardiac injury"				
Gene ontology (GO) term	**# of genes**	**Normalized enrichment score**	**NOM p-value**	**FDR q-value**
Positive (10)				
mitochondrial protein complex	62	1.88	0	0.17
cellular respiration	59	1.83	0	0.11
regulation of cardiac conduction	23	1.83	0	0.09
Negative (430)				
extracellular matrix	125	−2.09	0	0
cell chemotaxis	37	−2.04	0	0
cytokine activity	57	−1.93	0	0.02
angiogenesis	89	−1.91	0	0.02
neurotransmitter transport	44	−1.86	0	0.03
integrin binding	29	−1.86	0	0.03
transforming growth factor beta receptor binding	15	−1.85	0	0.03
leukocyte migration	75	−1.85	0	0.03
regulation of extrinsic apoptotic signaling pathway	48	−1.84	0	0.03
developmental cell growth	15	−1.83	0	0.03
Principal Component 4 – "acute post-infarct injury"				
Gene ontology (GO) term	**# of genes**	**Normalized enrichment score**	**NOM p-value**	**FDR q-value**
Positive (443)				
myeloid leukocyte migration	18	2.23	0	0
immune response	253	2.2	0	0
regulation of inflammatory response	81	2.14	0	0
leukocyte activation	115	2.14	0	0
cell chemotaxis	37	2.13	0	0
lymphocyte activation	95	2.12	0	0
regulation of immune response	207	2.1	0	0
regulation of response to wounding	110	2.09	0	0
innate immune response	122	2.06	0	0
extracellular matrix	125	2.05	0	0
Negative (33)				
oxidative phosphorylation	40	−1.8	0	0.13
regulation of neurotransmitter secretion	15	−1.77	0	0.14
cellular respiration	59	−1.69	0	0.2
(#) - total number of terms with p<0.05, FDR<0.25.				

*Sample sizes and the details of statistical analyses were listed in the Fig. 2 legends.